Burial performance between different head shapes and skulls amongst head-first burrowing fishes

Marcos Martinez

A thesis submitted in partial fulfillment of the requirements for the
Master's degree in science

Department of Biology
Faculty of Science
University of Ottawa

Abstract

Burrowing is most energy costly behavior. Many vertebrates burrow head-first into the sediment. Interestingly, head-first burial fishes differ in head shapes by having either a flatten or conical head shape. Head shape determines the penetration force magnitudes, but it is important for their neurocranium to avoid overwhelming cranial stresses from those burial forces. There is minimal research on the penetration force (N), rotational resistance (Nmm), and cranial stress (Pa) for different head shapes. Here, we selected four members with different head shapes: *Tetraodon miurus* (Bulky), *Iniistius pavo* (knife edge), *Bunocephalus coracoideus* (shovel), and *Cheilio inermis* (knife point). We constructed 3D head shape models and controlled the surface areas. We recorded penetration force (N) and torque (Nmm) for each model. We also constructed the neurocranium models and loaded them in Finite Element Analysis (FEA) to examine the stress magnitudes and concentrations. Our results show that bulky penetrated with highest penetration force, and knife point and shovel penetrated the minimum force. Knife edge experienced the greatest sediment resistance. Knife point succumbed to highest stress magnitude. The premaxillae and maxillae were the bones constraining burial for shovel. The parasphenoid bone constrained knife edge, knife point, and bulky during burial. From our results, having larger wide head dimensions and larger volumes generated greater penetration forces. Those with a flatten head succumbed to high sediment rotational resistance. Bone arrangements influences stress magnitudes because those with different skull shapes, yet same bone arrangements were constrained by the same bone. It seems there is a tradeoff between penetration force and cranial stress magnitudes. Fish use their parasphenoid for feeding and burial for those in our study, so there may be relationship between burial and feeding.

Acknowledgments

I want to thank my advisor, Dr. Emily Standen, for welcoming me to Canada and giving me a chance to pursue a MSc in BioMechanics. Thank you for your patience, kindness, and guidance throughout my time here in uOttawa. I also want to thank my committee members, Dr. Kathleen Gilmour and Dr. Michel Labrosse, for their support and advice.

Thank you to my parents for their love and support, and for introducing me to the sport of fishing as a child which ignited my passion into fish biology. Thank you to my brother for being supportive and being the best brother, anyone could ask for. In addition, thank you to my current and former lab mates for their support and welcoming me to Canada as well.

Table of Contents

List of Figures

List of Tables

Chapter 1: Research background

1.1. Introduction

Burrowing occurs when animals push into the substrate to permit entry (Broek and Rice, 1975; Dorgan, 2015; Herrel et al., 2011; Maladen et al., 2009). Burrowing animals reside within soils and sediments that cover most aquatic sediment and terrestrial substrates (Dorgan, 2015). Evidence of burrowing initially appeared in the fossil record at the end of the Precambrian. At this time, the microbial mat covering the sediments was dominated by primitive sessile invertebrate burrowers that resided within both microbial mats and the substrates beneath (Meysman et al., 2006). Burrowing behavior has diversified across many animal phyla, and there are diverse burrowing motivations, burial modes, and body shapes (Dorgan, 2015). Both vertebrates and invertebrates burrow to avoid or aid predation (Bilecenoglu, 2013, Lewis, 1976), to rest and sleep (Tatom-Naecker & Westneat, 2018; Videler, 1986), to construct tunnels (Able et al., 1982), to estivate (Carlson, 1968), and to regulate temperature (Benesch and Withers, 2002). Animals burrow using head-first burrowing (Bergmann and Berry, 2021; Gidmark et al., 2011, Herrel et al., 2011; Maladen et al., 2009; Tatom-Naecker and Westneat. 2018) tail-first burrowing (Herrel et al., 2011; De Schepper et al., 2005), vertebral torsional burrowing (Young and Morain, 2003), and scratch-digging (Lin et al., 2019). There are morphological distinctions between burrowers depending on their motivations and burial modes. Terrestrial vertebrates with limbs evolved wider forelimb digit's surface area and are equipped with powerful muscles to facilitate pushing against the soil (Lin et al., 2019). In contrast, limbless animals employing head-first burrowing are equip with a mechanically suitable skull to withstand the penetration forces (Herrel et al., 2011; De Schepper et al., 2009).

Most burrowers share the common morphological trait of a smooth exterior. Mammals have soft hair (Lin et al., 2019), fishes and reptiles can have smooth scales or even be scaleless (Bizzaro et al., 2016; Gidmark et al., 2011; Maladen et al., 2009; Steendam et al., 2020), and many burrowing invertebrates have smooth exoskeletons (Alexander et al., 1993; Sassa et al., 2011; Trueman, 1966).The convergence of smooth integument found across burrowing taxa may result from high magnitudes of frictional drag experienced when burrowing through granular media (Alexander et al., 1993; Ding et al., 2012). Granular media is a complex environment because it is a dilatant fluid where increasing the shear stresses and rates within the substrate increases compaction that makes burrowing difficult (Frazini et al., 1997; Pradhan et al., 2019). This unstable media requires burrowers to generate adequate mechanical power to penetrate through the substrate and maneuver within it (Ding et al., 2012; Dorgan et al., 2005; Dorgan, 2015). Frictional drag and therefore penetration forces are minimal at the sediment superficial layer but increase with increasing substrate depth (Ding et al., 2012). Sediment particle shape affects force dependence; angular particles, that are prone to high compaction gradients, require greater forces to penetrate compared to spherical particles (Bergmann and Berry, 2021). In addition, larger particle diameters require higher loads to penetrate through than smaller particle diameters resulting in some fishes being able to bury themselves rapidly in fine and medium grains but not in coarse particles (Mckee et al., 2016; Steendam et al., 2020; Stoner and Ottamar, 2003).

In a study that examined the relationship between respiration rate and work performance, burrowing requires 350 times more energy than surface locomotion (Wu et al., 2015). Because of the energy required to bury, animals have developed different behavioral tactics to minimize the force required to burrow. One tactic is substrate fluidization, and this occurs when animals push a fluid (water or air) into the substrate to reduce compaction or suspend particles into the fluid column that then settle over the animal aiding the burial process (Dorgan, 2005; Lewis, 1978, MacDonald, 2005). Experiments that looked at performance metrics in lizards moving through sediment in differing compaction gradients, found that animals moved more slowly and used less force in compacted substrate compared to when they moved through a fluidized bed of non-compacted substrate (Ding et al., 2012; Maladen et al., 2011). In the wild, sandfish (*Trachinus trachinus),* burrow by rotating their pectoral fins to scoop sand in conjunction with a ventilatory pump which expels water from their gills into the sediment near the pectoral fins, potentially reducing granular compaction (Lewis, 1978). Researchers speculate that burrowing bivalves also fluidize the substrate which reduces the amount of force required to bury and allows them to maintain a consistent force output as they descent into the substrate (Sassa et al., 2011). Another behavioral tactic is adjusting sediment entry angles. Both burrowing lizards and elongated bivalves burrow at smaller entry angles in compacted media and at larger angles in less compacted media, suggesting animals are altering their behavior to minimize forces required to enter the sediment (Maladen, 2009; Maladen et al., 2011; Sassa et al., 2011).

Because of the mechanical constraints involved with burial, we would expect that animals occupying the same environment, performing the same behavior, and having a similar burial mode would have similar morphologies. Within head-first burrowing fishes, this appears not to be the case. There are two head-first burial modes in fishes; 1) forceful plunging mode where animals quickly drive themselves into the substrate, which consists of high tail-beat frequency and low tail amplitude, and 2) slow wiggling mode, which consists of low tail-beat frequency, and high tail amplitude (Gidmark et al., 2011; Tatom-Naecker and Westneat. 2018). Both modes can be used at different times in the same burial event (Bileciglou et al., 2013; Gidmark et al., 2011; Herrel et al., 2011; Tatom-Naecker and Westneat. 2018); however, distinct morphologies are associated with fish that prefer one mode over the other. Fish that employ forceful plunging generally possessed an oval body shape (Tatom-Naecker and Westneat. 2018), and those who employ slow wiggling have elongated bodies (Herrel et al., 2011). It was hypothesized that forceful plunging requires stiffer bodies whereas slow wiggling requires flexible bodies (Herrel et al., 2011; Tatom-Naecker and Westneat. 2018). In addition to differences between body shape, there are differences in head shape among the head-first burrowers. How head shape is associated with burial mode and impacts burial performance is the focus of this thesis. Four different head shapes were selected in this study (Fig. 1.1, 1.2); the knife point (*Cheilio inermis*), which is a conical shape, tapered at the snout; knife edge (*Iniistius pavo*), which is a laterally compressed shape, tapered along the forehead and snout; bulky

(*Tetraodon miurus*), which is a larger head shape that tapers quickly towards the snout; the shovel (*Bunocephalus coracoideus*), which is a broad posteriorly and dorso-ventrally flattened head shape (Fig. 1.2). Using physical models of the four head shapes and a Universal Testing Machine, this thesis examines how head shape influences torque and axial force loading during burial (Chapter 2). In addition, Finite Element Analysis of compressive and tensile force loading elucidates what areas on the skull are most susceptible to force loading between different skull shapes (Chapter 3).

1.2 Figures

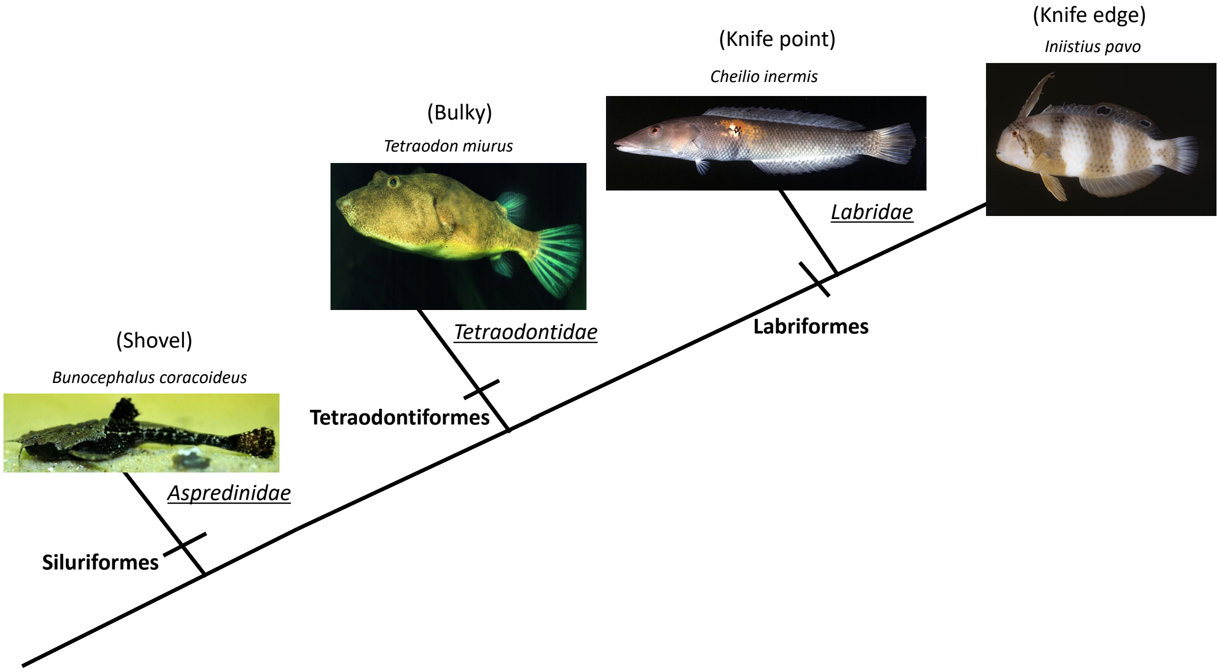

Figure 1.1: Phylogenetic relationship between head-first burrowing fishes used to produce models in this paper. Both *I.pavo* (knife edge) and *C.inermis* (knife point) images were obtained from FishBase. Images of *B.coracoideus* (shovel) and *T.miurus* (bulky) were obtained from (planetcatfish.com) and (Aquaterra-diffusion.fr), respectively.

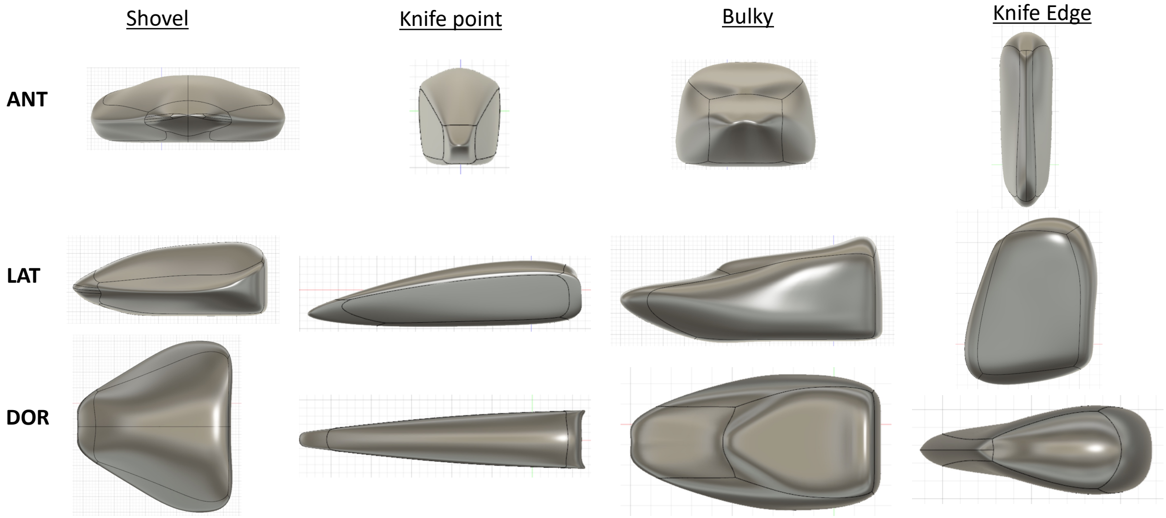

Figure 1.2: The four views of each head shape from Autodesk Fusion 360. Models after successfully sculpting them with the anterior (ANT), lateral (LAT), and dorsal (DOR) from Fusion 360 with *B.coracoideus* (shovel), *C.inermis* (knife point), *T.miurus* (bulky), and *I.pavo* (knife edge).

Chapter 2: Effect of head shape on head-first burial force production in fishes.

2.1 Introduction

To understand how head shape influences burial performance, it is important to understand the forces that different shapes elicit when pushed through sediment. Conical shapes exert less force than spheres and disks when pushed into the substrate (Brzinski et al., 2013; Clark and Behringer, 2013). This may explain why many head-first burrowing lizards and fishes have evolved conical head shapes (Bergmann and Berry, 2021). Physical models have been used to imitate various head slopes, pointiness, and diameters, and have found that diameter has the greatest impact on penetration force production whereas head slopes and pointiness have little to no effect (Bergmann and Berry, 2021). As would be expected, shapes with wider diameters have higher force production during penetration (Bergman and Berry, 2021). Unexpectedly, no matter the head shape, penetration forces are not correlated with the rate of entry (Albert et al., 1999; Katsugari and Durian, 2013; Stone et al., 2004). To date, models have been highly effective in determining important physical principles associated with burial. Some of the most detailed studies, however, use models that are tetra-radially symmetric which may not apply to the bilaterally symmetric shapes of biological animals who bury. This chapter aims to use bilaterally symmetric models of actual fish head shapes to understand how biologically relevant head shape influences force production during burial.

Fish are a remarkably diverse group of vertebrates and across their phylogenetic tree many different groups burrow in many ways. For the purposes of this study, we have chosen four different species that represent head-first burrowers, distributed across the fish phylogenetic tree, to compare functional performance across four different head shapes: shovel, bulky, knife point, and knife edge. Except for knife point and knife edge which are both from the *Labridae* family, these examples come from diverse orders of fish with varying burrowing life history patterns (Fig 1.1). Very little work has been done on fish burrowing behavior for each of the model species we have chosen for this work.

Shovel shaped head (*Bunocephalus coracoideus*)

The shovel shaped head is dorso-ventrally flattened head that tapers to the snout (Fig. 1.2). Our shovel shaped head is represented by *Bunocephalus coracoideus*, a member of the *Aspredinidae* family of the order Siluriformes. Fish in the *Aspredinidae* family that burrow head-first do so to evade predators, and they are equipped with stiff bodies that are rigid in the caudal region compared to non-burrowing members of the family (Roberts, 2015). In the water column, they swim by undulating their body while simultaneously ejecting water through their opercles to propel themselves forward (Le Bail et al., 2000). This specimen was selected because it has a depressed head shape that resembles a shovel-like head shape. There is limited research on how many *Aspredinidae* members head-first burrow.

Bulky shaped head (*Tetraodon miurus*)

Bulky head shapes are generally large in all three dimensions (Fig. 1.1; 1.2). This shape of head is found in the *Tetraodontidae* family of the order Tetraodontiformes (Fig. 1.1). Only a few species in the *Tetraodontidae* burrow, and there are limited studies on how many species head-first burrow (Bilecigelou, 2013). Most burrowing *Tetraodontidae* are ambush predators. They head-first burrow to position themselves just under the substrate surface to have their mouths exposed for ambushing prey (Bilecigelou, 2013). *Tetraodontidae* generally have stiff bodies with a thick dermis and rigid skeleton (Brainerd, 1994), and they usually swim by undulating and oscillating their median paired fins for propulsion (Webb, 1984). A few *Tetraodontidae* members head-first burrow (Bilecigelou et al., 2013), but they generally are equipped with the same overall head shape.

Knife point and knife edge shaped heads, *Cheilio inermis* and *Iniistius pavo*, respectively.

The knife point is a conical head shape that comes to a single point at the snout while the knife edge is a laterally compressed head shape that comes to a thin edge from forehead to snout. These two head shapes are found in the more derived *Labridae* family in the order Labriformes (Fig. 1.1). The family *Labridae* contains roughly 500 species of fish, which propel themselves by oscillating their pectoral fins at slower speeds and switch to body undulatory movements to swim rapidly (Sfakiotakis et al., 1999; Webb, 1984). Nearly half of all *Labridae* fishes are burrowers, all of which use the head-first burrowing mode and do so to sleep or evade predators beneath the substrate (Videler, 1986). Although they are morphologically diverse, *Labridae* fishes that burrow tend to have two different head shapes, the knife point, and the knife edge (Videler, 1986). The knife point appears to be the ancestral head shape with more derived species acquiring the knife edge shape; however, some *Labridae* members which are not burrowers possess knife edge head shapes as well (Tatom-Naecker and Westneat. 2018). Although many head-first burrowing *Labridae* members are equipped with a knife edge head shape, *I.pavo* had the steepest frontal head profile angle amongst its' knife edge relatives (Tatom-Naecker and Westneat. 2018) which is the reasoning for *I.pavo* being selected for this study. The knife point, *C.inermis*, was selected because it has a slender, elongated, and conical head shape that has a low frontal profile head angle.

No matter the head shape, head-first burrowers employ a compressive force to penetrate through the substrate which represents an axial force on the skull and body of the fish (Dorgan et al., 2015). In addition, burrowing can require torque or twisting forces. It is known that some burrowing snakes employ a long-axis vertebral torsion along their bodies to burrow vertically into the substrate (Young and Morain, 2003). Because fish lack cervical vertebrae, head-first burrowing fishes may rely on long-axis vertebral even more so as they have limited lateral side to side head motion (sandlance - Gidmark et al., 2011). How axial and torque forces differ between biologically relevant head shapes is not known. Here we constructed bilaterally symmetrical physical models to test how axial and torque force production changes between different biologically relevant head shapes seen in burrowing fishes.

We hypothesize that different head shapes with same surface area will have different axial and torque forces. Based on profile, we predict that bulky heads will produce the largest axial forces followed by the shovel shaped, knife edge, and knife point each producing less force respectively. Specifically, we predict that all head shapes will have similar low force production at the snout (10%) with differences in force production across head shapes increasing with burial depth due to increases in the bulk of the head shape. We also predict that torque forces will be highest in the shapes that have greatest surface area to volume ratio (knife edge and shovel head shapes) followed by the shapes with lower surface area to volume ratios (bulky and knife point head shapes). We predict too that there is an interaction between axial and torque forces such that twisting will aid in the reduction of forces during axial descent into the substrate.

2.2 Material and Methods:

2.2.1 Specimens

All species that were selected use a head-first burrowing style. Species came from three orders of fish each with a different cranial morphology: Labriformes - *Inistiius pavo* and *Chelio inermis* of the *Labridae* family, Tetraodontiformes - *Tetraodon miurus* of the *Tetraodontidae* family, and Siluriformes - *Bunocephalus coracoideus* of the *Aspredinidae* family where all belong to Teleosts class (Fig 1.1 and 1.2).

2.2.2 Head shape modeling and printing

I.pavo, C. inermis, B. coracoideus , and *T. miurus* were modeled using the Autodesk Fusion 360 student version 2.0.12670 (www.autodesk.com). Before modeling, we uploaded dorsal, lateral, and anterior views of each head. Intact or fleshed head images were optimal, and intact head lateral views of all species were available through fishbase. Fleshed out anterior and dorsal images were difficult to find for most of these species, so we compensated by using CT scans to model each head shape. This was completed by downloading CT scans of all specimens from MorphoSource, loading them to 3DSlicer and taking anterior and dorsal screen shots of each scan (Buser et al., 2018). All fleshed and CT images were loaded into Fusion 360 scaled with each other and oriented to appropriate axes for subsequent modeling (Fig. 2.1). After each head was modeled a spectro or UTM attachment was fitted to the point of cervical attachment (Fig. 2.2). Each head shape was scaled to 750mm^2 surface area excluding the spectro piece. After the spectro was added, we exported each head shape models as a STL file for 3D printing.

We individually 3D printed the head shapes at the uOttawa Makerspace. The STL files were loaded on Ultimaker Cura version 4.7 (https://ultimaker.com/software/ultimaker-cura), and the 3D print settings were 50% fill, 3 mm walls, and printed with a 0.4 mm nozzle. The print material was PLA, Poly Lactic Acid. After the 3D prints were done, we smoothed the surfaces with a light sanding because the natural specimens have smooth skin by nature.

2.2.3 Sand box modeling and printing

The cylinder used to contain the sand into which the heads were driven was made of two parts; a rectangular prism base that sat on the UTM plate and a cylindrical container which was glued to the prism base. The rectangular prism base had dimensions of 15 x 15 x 1.5 cm (L x W x H). The cylindrical sand container had an inner diameter of 19 cm, height of 12 cm, and a wall thickness of 0.25 cm (Fig. 2.4). Both pieces were individually 3D printed with PLA, 50% fill, and 0.8 mm nozzle then subsequently glued together. The rectangular prism indentation was present to fit the UTM plate inside it. The appropriate cylinder inner diameter (19 cm) was calculated to be ten times larger than the largest head dimension which is proven to reduce edge effect during testing (Bergman and Berry, 2021). The depth of the sand was set to 8 cm, which based on data collected on similarly scaled tetrahedral shapes resulted in negligible bottom effects (Bergman and Berry, 2021).

2.2.4 UTM Trials

The sand container was filled to a height of 8 cm with a heterogenous mixture of dry medium sized particles of 0.25-1 mm diameter (median of 0.53 mm), and particle shapes were angular and spherical. The Zwick Roell's universal testing machine (UTM) static applications model was used to measure axial and torque forces. The UTM measures axial forces (N) by driving the head models vertically downward into the sediment. Torque (Nmm) is measured by the head models' turning resistance at and beneath the sediment surface. The vertical rate of entry was set at 150 mm$(\mathrm{min})^{-1}$ and heads were rotated 50 deg at 250°$(\mathrm{min})^{-1}$, clockwise and then counterclockwise repeatedly. Head descent paused at 10% BL (body length) increments until the full 50° rotation was complete. This allowed us to measure rotation with and without axial loading.

Both axial and torque force measurements were terminated when the head reached 100% penetration into the substrate. The models were slightly above the sediment and positioned above the center of the sand box. We recorded five trials for each head shape. Between trials of the same model, we stirred and leveled the sand to avoid substrate compaction (Albert et al., 2000). Between models, we emptied and refilled the sand. We analyzed axial forces with torque, and torque forces during descent and no descent, for all head shapes (Fig. 2.3). In a separate trial, we also measured axial forces that were the result of descent without any rotation (Fig. 2.3). We examined the axial and torque forces of each head at 10, 30, 50, and 80 percent of head length.

2.2.5 Statistics

Differences in maximum axial force production (independent of rotational motion) during an entire penetration event for different head shapes was tested using a one-way ANOVA. A second one-way ANOVA was used to test differences in maximal torque force production (independent of axial motion) due to head shape. We used four, two-way ANOVAs to analyze (1) how head shape and rotational mode (no twist / twist) affected axial force production, (2) how head shape and descent mode (descent / no descent) affected torque force production (3) how burial depth (in percentage head length) and head shape affected axial force production independent of rotational motion and (4) how burial depth and head shape affected torque forces independent of axial motion. Multiple comparisons were made using Tukey tests. Significance was determined using P-values of 0.05. All statistical tests and plots were done in RStudio version 1.4.1103.

2.3 Results

2.3.1 Axial and torque production in isolation

When head shapes were pushed into the substrate without rotation, maximal axial force production was lowest in shovel and knifepoint head shapes and highest in the bulky head shape (Fig. 2.5; Table 2.1 One-way ANOVA). When torque forces were measured in isolation from axial forces, maximum torque forces were highest in the knife edge head shape followed by knife point, bulky and shovel head shapes (Fig. 2.5; Table 2.1; One-way ANOVA).

2.3.2 Changes in torque and axial forces with burial depth

Torque forces were measured in isolation from axial forces at 10, 30, 50 and 80% burial depths. Torque force production remains constant with increasing burial depth for all head shapes except for knife edge head shape where it increases with depth into the substrate (Fig. 2.7; Table 2.2). For all head shapes axial force production increased with burial depth (Fig. 2.6; Table 2.3). At the start of burial (10% burial depth) there were no differences in axial force production between head shapes (Tukey, $p > 0.05$). At 30% burial depth into the substrate, the bulky head shape experienced greater axial force than knife edge head shape (Fig. 2.6; Table 2.3; Tukey, $p < 0.05$). At 50% and 80% burial depths bulky head shape experienced greater axial force than all other head shapes (Fig. 2.6; Table 2.4).

2.3.3 Axial and torque force production combined

When heads were rotated during axial force loading, axial forces decreased dramatically for bulky, shovel, and knife edge head shapes but not for knife point head shape (Tukey, $p < 0.05$;

Fig.2.8; Table 2.4). For all models, the torque force output did not change with axial loading (Fig. 2.9; Table 2.4), however knife point head shape showed a decreasing trend (Fig. 2.9).

2.4 Discussion

The purpose of this study was to understand how torque (Nmm) and axial (N) force productions during burial differs between different head shapes. Four different head shapes that are found in head-first burrowing fishes were used in this study. We also examined how torque loading affects axial forces, and how axial loading affects torque force production. We assume there to be an evolutionary advantage to minimizing forces experienced by burrowing fishes as it would reduce potential energy expenditure and minimize tissue failure during burial.

2.4.1 Isolated axial and torque forces and the substrate displacement hypothesis

Although it may be rare that an animal burrows with completely isolated axial or torque forces, it is interesting to understand how these forces change independently from each other to understand the mechanical principles acting on the system. In all cases, movement through a substrate is dictated by two types of drag forces, frictional drag that involves forces that are parallel to the surface of the animal and increase with surface area, and profile or form drag that involves forces that are perpendicular to the object surface and are dictated by shape (Biewener and Patek, 2018; Zhang and Goldman, 2014). Axial and torque forces are the result of both friction and form drag in different ratios. Given these physical principles, the surface area, volume, and shape of an object will determine how axial and torque forces develop against the substrate, and also within the skull (Covey and Greaves, 1994; Cuff and Rayfield, 2013).

Our data, unsurprisingly, shows that axial loading increases with burial depth across all head shapes (Fig. 2.6). This can be explained by both an increase in the surface area of the object in contact with the substrate (increased frictional forces) as well as the amount of substrate that needs to be displaced by the object as it dives into the soil (increased displacement or form induced forces) (Zhang and Goldman, 2014). Earlier work that looked at several shape and size parameters in rods pushed into substrate showed that rod diameter was the most important factor that influenced force magnitudes (Bergmann and Berry 2021). Because point slope and point sharpness in this past study had little effect on the force magnitudes experienced by the rods driven into the substrate, one might surmise that the aspect of diameter that was most influential was the volume the rod displaced rather than its shape. In our data, we attempt to test this 'substrate displacement hypothesis' which suggests that burial force loading is determined by the amount of substrate being displaced rather than the surface area of the object entering the substrate. In our experiment we controlled for surface area, all head models had a 750 mm^2 surface area but, because of shape differences, they differed in head volume (Table 2.5). Our data supports the 'substrate displacement hypothesis' as we see bulky and knife edge head shapes which have the highest head volume experiencing the largest axial forces during penetration (Fig. 2.5).

The 'substrate displacement hypothesis' is also supported by our isolated torque loading data. In our data, the knife edge head shape experiences the highest torque loads but is not the shape with the highest volume (Fig. 2.5; Table 2.5). Although our results may appear contrary to our predictions, with maximum head volume not aligning with maximum torque force production, this can be explained quite easily with the concept of 'added volume'. In twisting, given two objects with different shapes but with the same volume, a flat plate will displace more substrate than a rod, as it twists (in fluids problems this is called 'added mass' and can be roughly estimated by calculating the volume of a sphere that has the same projected surface of the object accelerating in each direction (Brennan C.E., 1982). Essentially, the plate, in motion, gains dynamic volume as it accelerates the substrate it must move, and so requires more force to spin. Our data shows that the knife edge shape, although not the shape with the largest volume, experiences the largest forces in torque. Also, the bulky shape, although containing the highest volume, is round enough to minimize 'added volume' reducing the amount of torque force required to spin (Fig. 2.5).

2.4.2 Combined axial and torque forces and the substrate compaction hypothesis

One anomaly does present itself in our data. If we were to look at the characteristics of the knife point shape within the context of the 'substrate displacement hypothesis' it has both the lowest absolute volume of all the shapes tested and the lowest 'added volume' in terms of its height to width ratio (it is almost a perfect circular rod). With these characteristics and our above reasoning, we would expect that the knife point shape would have the lowest axial and torque force production when driven into the substrate, however, this is not the case (Fig. 2.5). This lack of congruency leads us to a second 'substrate compaction hypothesis based on the geophysical principle that as you go deeper into the sediment, sediment becomes more compacted (Ducey et al., 1993; Sharpe et al., 2013). We would then predict that head shapes of similar size, but longer in the axial direction would drive deeper into the substrate and thus experience higher axial and torque burial forces due to compaction of the substrate (Sassa et al., 2011; Sharpe et al., 2013). This prediction would explain the unexpectedly high forces experienced by the knife point head shape.

The 'substrate compaction hypothesis' also helps to explain the behavior of our data when axial and torque forces are examined in combination. Interestingly, if head shapes are turned while they are pushed into the soil (simultaneous rotational and axial motion) axial forces decrease significantly for most head shapes (Fig. 2.8). This suggests that the increase in motion and associated torque forces disrupts the substrate facilitating penetration as the head descends. Many fish use fluidization of substrate to facilitate burial which acts on a similar principle (Dorgan, 2015; Lewis, 1976). By disrupting the sediment, compaction is reduced, and it becomes easier to drive into the ground. Twisting contributes torque forces, possibly loosening sediment, reducing compaction, and reducing the forces required to penetrate axially into the soil (Young and Morain, 2003). Our data also shows that torque forces are not changed with the addition of downward axial motion (Fig. 2.9). Because the transfer of force reduction is unidirectional (i.e. rotational motion can decrease axial force loading but axial motion does not reduce torque forces) and because we know that soil compaction increases with substrate depth, our data further supports the idea that rotational motion is facilitating substrate de-compaction. Further evidence of this physical process is supported by the fact that the knife point shape did not experience a reduction in axial loading when rotational motion was added. Based on its almost perfectly round cross-section, the knife point shape has a very small ‘added volume’ component to its twisting motion, this means that very little substrate motion will occur limiting the substrate de-compaction and providing no reduction in axial loading upon descent (Fig. 2.9).

2.4.3 How burial relates to life history in fishes

The bulky head shape experienced the highest axial forces when entering the substrate at 90˚ to the surface. This could be detrimental to the integrity of the fish skull. The fish, *T.miurus*, that supports the bulky head shape burrows to ambush prey, so they lie slightly beneath the substrate surface exposing their mouth and eyes. It was observed that these and related fish in in the *Tetraodontidae* family generally burrow at low sediment entry angles. By reducing sediment entry angles, fish may minimize forces experienced upon the skull. This could be a universal tactic to lower forces experienced during burial as the terrestrial sand lizard, *S. scinus,* is also equipped with a knife point head shape (like the Labridae fish, *C. inermis*) that generally burrows in low sediment entry angles (< 45°) (Sharpe et al., 2013).

The head shape and size of the animal and with speed which it moves affects their burial strategy (Bergmann and Berry, 2021; Hosoi and Goldman, 2015). Head shape may evolve with body stiffness. In our study, head shapes that experienced the highest burrowing forces (bulky and knife edge head shapes) were found in fish that also had the greatest body stiffness. Perhaps when a head shape requires higher axial forces to penetrate through the substrate, body anatomy must accommodate by stiffening to allow axial swimming forces to more effectively be passed to the head.

2.4.4 Influence of axial and torque forces on animal burial

Our data shows that adding torque loading during burial is advantageous as it reduces axial forces. Bulky, knife edge, and shovel head shapes dramatically reduced their penetration forces when adding torque (Fig 2.8). The only shape that did not benefit from reduced axial loading when twisted was the knife point head shape (Fig. 2.8). Although knife edge head shape reduced axial forces when twisting, they experienced very high torque loads in the rotation. Interestingly, the shovel head shape, that has a similar medio-lateral shape to the knife edge dorso-ventral dimension does not experience the increase in torque forces. The difference could be explained because the knife edge head shape reaches a greater dorso-ventral dimension sooner than that of shovel head shape, so at full penetration, the knife edge head shape is interacting with more compacted sediment and causing an increase in the torque load. The increase in torque loading of the knife edge head shape may be problematic and so fish with this shaped skull may use other behavioral tactics to reduce their force dependence such as fluidization (Dorgan, 2015; Sharpe et al., 2013; Sassa et al., 2011) and adjusting their sediment entry angles (Sharpe et al., 2013; Sassa et al., 2011).

The 3D constructed head shapes were modeled using one set of physical and CT scan images, so each head shape had one 3D model representation with a single set of head dimensions.

Although, it would be optimal to obtain many physical specimens and photograph different head views to add biological variation to 3D models, this study provides critical information about the general impact of head shape on burial by comparing between representative head shapes across a biologically relevant range. The method we used to gather force and torque information from our head shapes was limited by the capacity of our UTM machine. Although it is unlikely or rare these specimens burrow in 90° sediment entry angles, we could not alter the sediment entry angle < 90°. In addition it would be interesting to quantify the difference in forces produced in dry compared with wet substrate but we did not have an appropriate containment device to protect the UTM machine from the potential effects of water.

2.4.5 Conclusion

The fact that surface area, volume and shape are intricately linked by geometrical laws suggests that there is a natural tradeoff between them. Additionally, the fact that shape has different impacts on axial vs torque forces creates a very wide and diverse selective landscape for head shape and burrowing behavior and helps to explain why we see such variation in head shape morphology across head-first burrowing fishes. Axial forces decreased substantially for most head shapes with torque loading, but the same cannot be said for axial loading upon torque recordings.

2.5 Figures

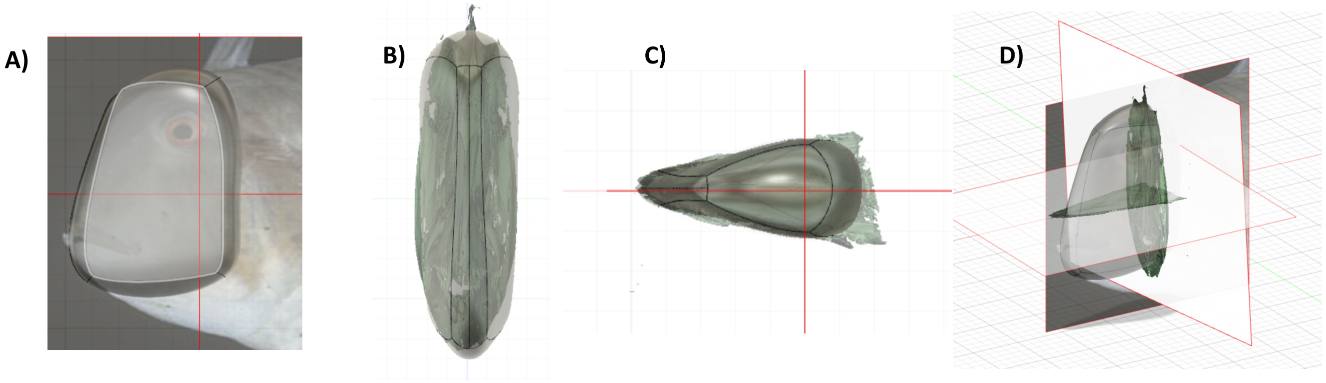

Figure 2.1: Model development train for *I.pavo* (knife edge). A) fleshed lateral image obtained from Fishbase has a simple form overlaid in AutoDesk Fusion 360 B) anterior view of head scaled to the geometric model form in Slicer3D, C) dorsal view and image of model superimposed from Slicer3D and D) includes all three views overlain into a 3D model.

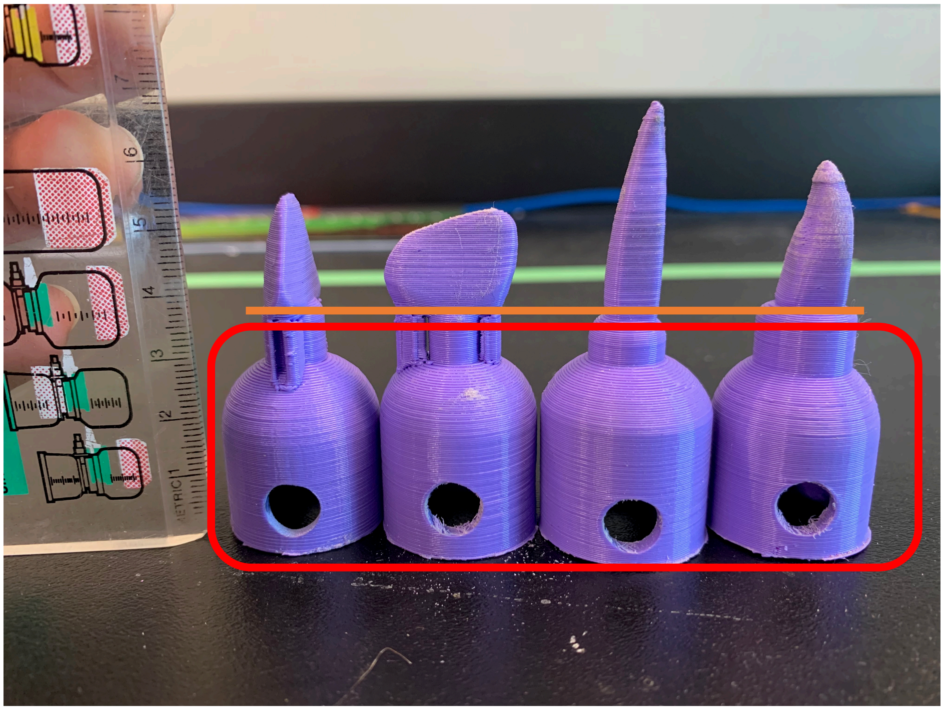

Figure 2.2: Physical models after 3D printing with their spectro attachment. This was their lateral side after 3D printing with the UTM spectro attachment (**red** rectangular outline). The **orange** line above the red rectangle is how deep the models went into the substrates. From left to right, shovel, knife edge, knife point, and bulky.

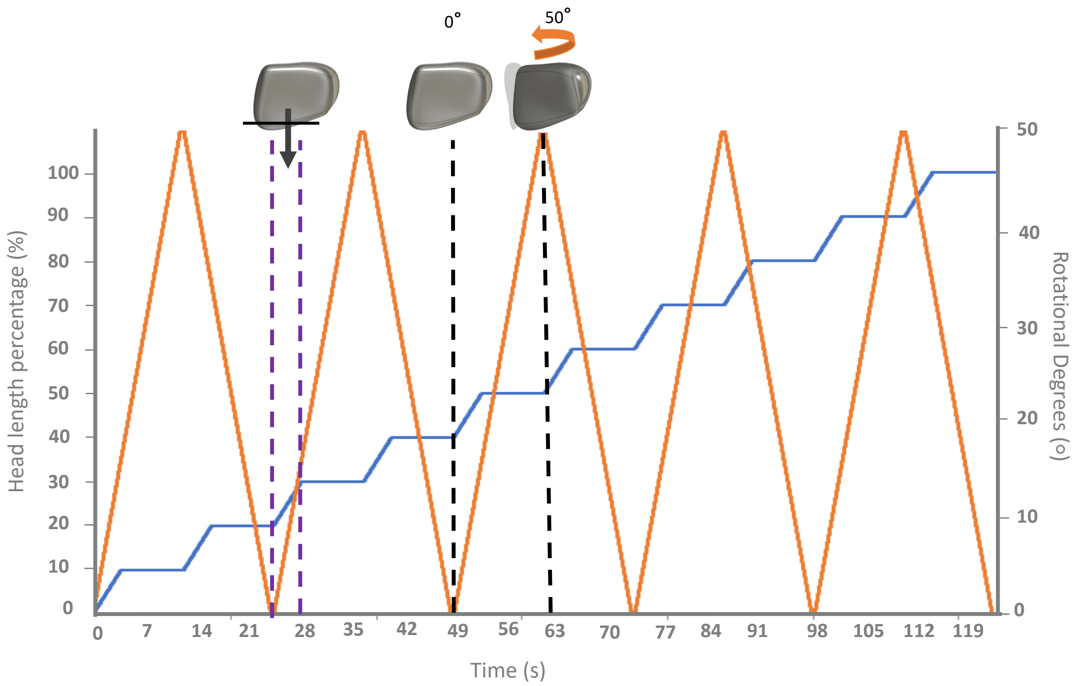

Figure 2.3: Example plot showing the axial loading and torque loading methods of the knife edge head shape. The **head length percentage** (%) on the y-axis represents the respective head length percentage embedded in the sediment. The secondary y-axis is **rotational degrees** (°) that fluctuates between 0° and 50°. The x-axis is time (s). The lateral side knife edge head shape from Fusion 360 with the downward arrow between the two **purple** vertical dash lines represents the model descending during that time. The flatten lines on the **head length percentage** line represents the models not descending. The head model above the **black** vertical dash lines are the model rotating from 0° to 50°, respectively, with the corresponding **orange** arrow showing the 50° rotation.

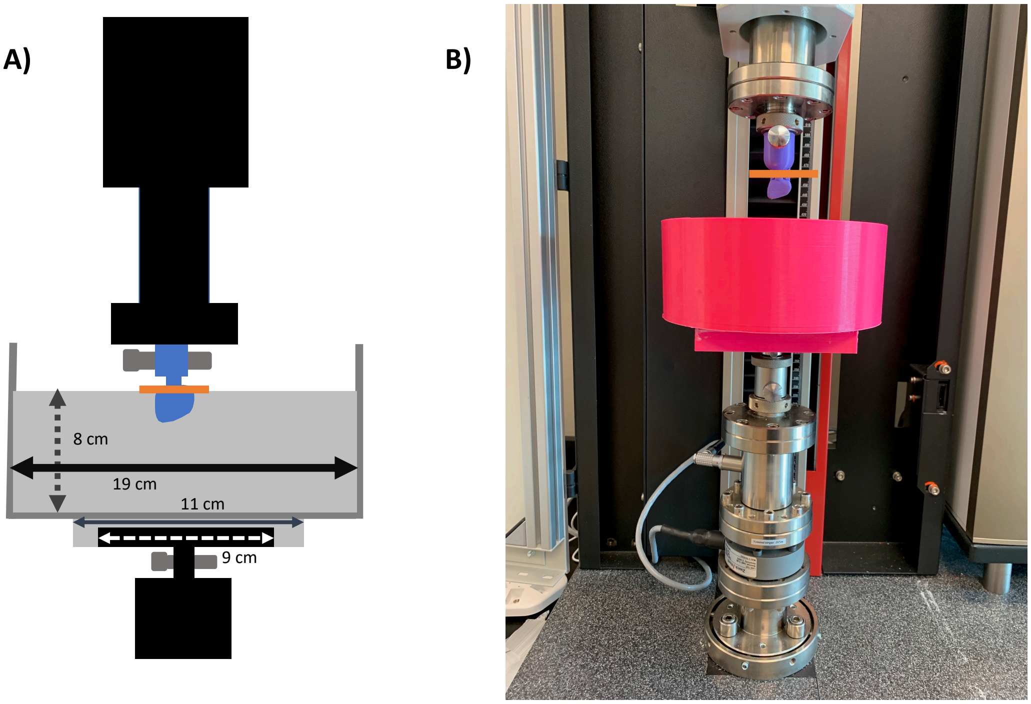

Figure 2.4: Experimental set up with the 3D printed models mounted to the UTM. A) schematic of the UTM machine with the sand box and head model mounted along with the physical set-up. The black solid line (19 cm) represents the inner diameter of the sand box, the dash vertical grey line was the substrate height 8 cm, and white dashed line just below was the square indentation of 9 cm whereas B) is the physical model with the head model and sand box mounted as the schematic version. The orange line was this head models' maximum substrate depth in both A and B.

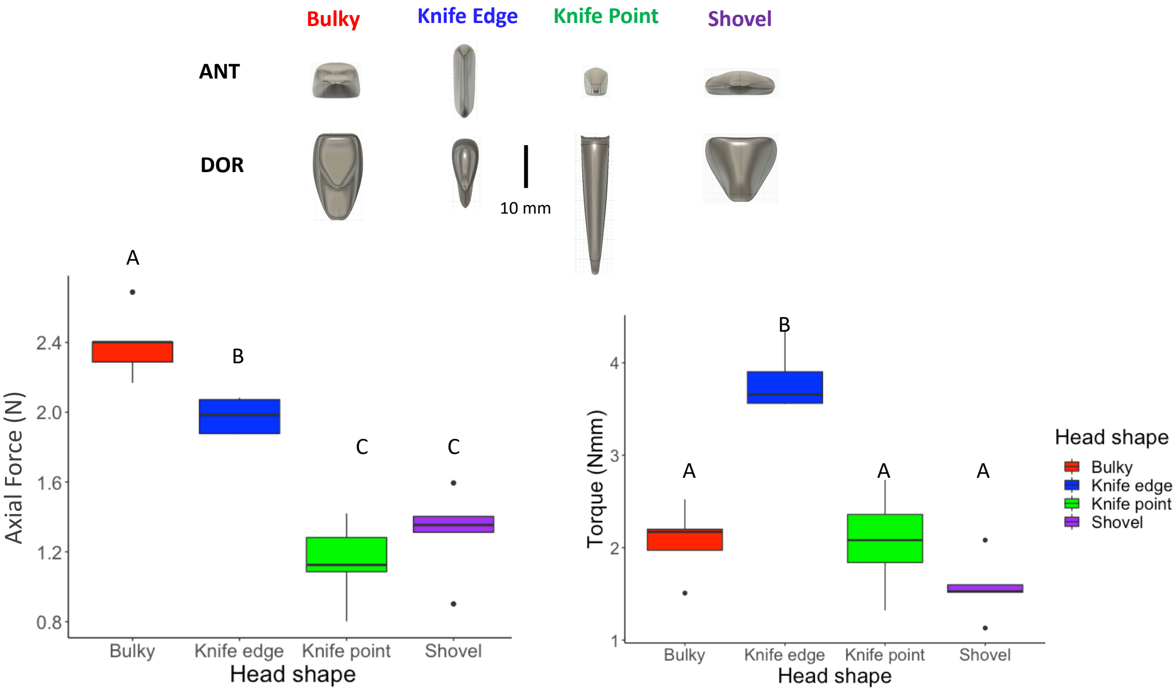

Figure 2.5: Total maximum isolated axial and torque forces for each head shape. Maximum isolated axial force is taken over the entire purely axial penetration cycle. Maximum isolated torque force is taken as the maximum force measured in purely torque motion at discrete 10% increments from 10% to 100% of burial depth. Anterior view (**ANT**) and the dorsal (**DOR**) view of head models color coded with **bulky**, **knife edge**, **knife point**, and **shovel**. (LEFT) maximum axial force and RIGHT) maximum torque force color coded with the head shapes. The letters in A) and B) represent Tukey multiple comparisons of the one-way ANOVA results. Similar letters are not significantly different (Tukey, $p < 0.05$). Each boxplot contains five recordings.

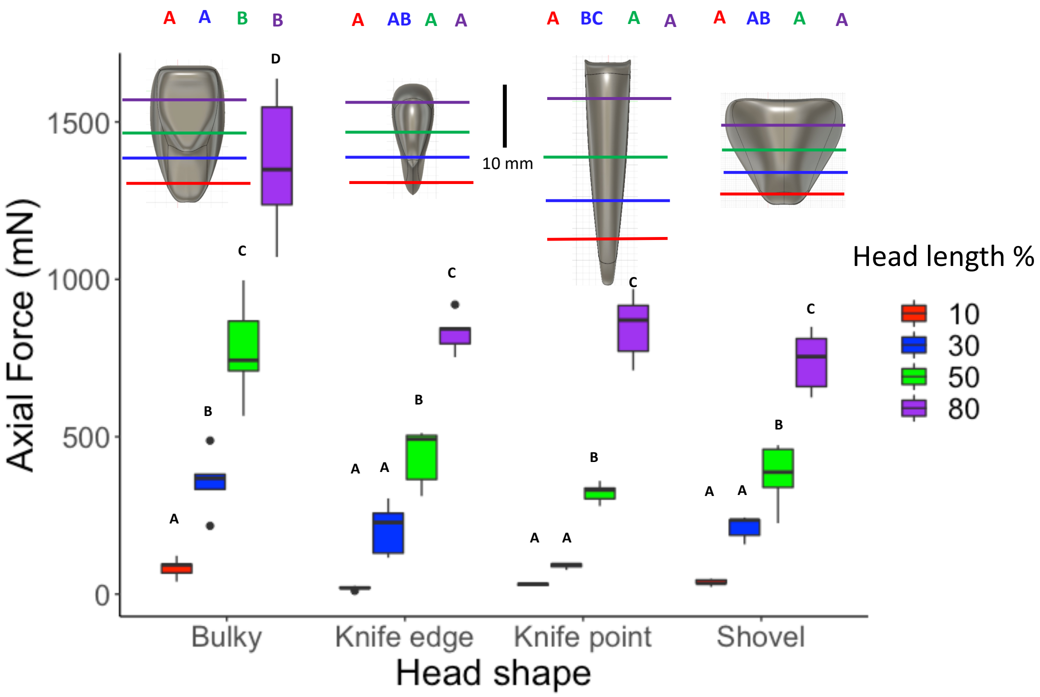

Figure 2.6: Axial force production at different burial depths within and across head shapes. The burial depth in percentage (**10%**, **30%**, **50%**, and **80%**) for the corresponding boxplots and position on dorsal view of each head shape. Within each head model different black letters above each boxplot represent significant differences in axial force production. Differences in the colored letters above the dorsal view images represent significant differences between head shapes at a given burial depth (compare only like colors; Tukey, $p < 0.05$). Each boxplot contains five recordings.

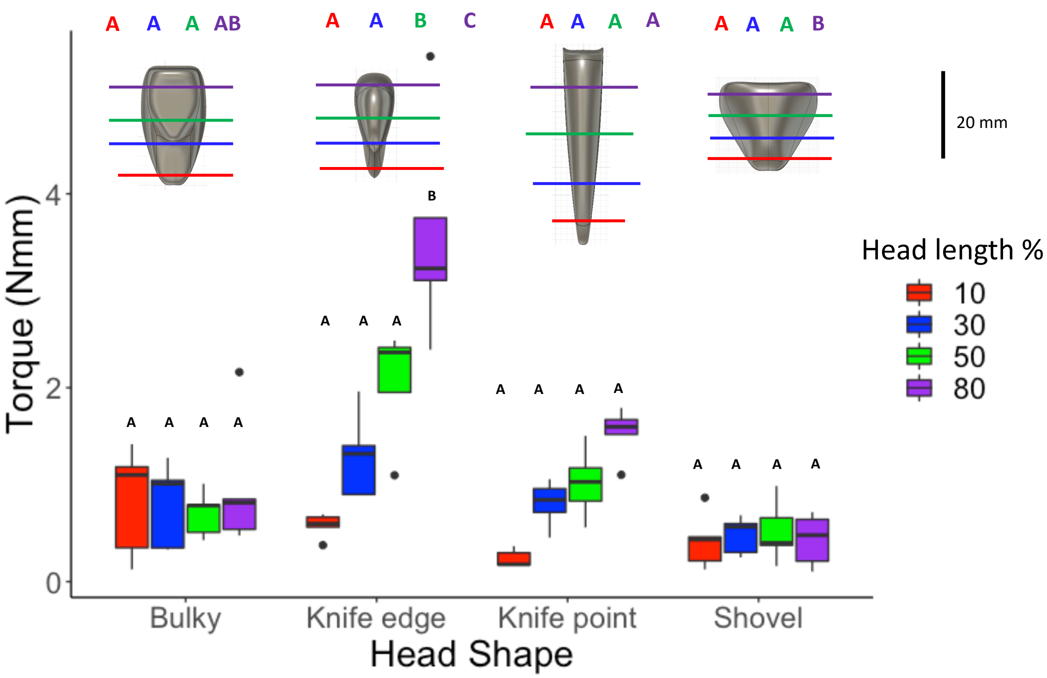

Figure 2.7: Torque force production at different burial depths within and across head shapes. The head lengths percentages colored (**10%**, **30%**, **50%**, and **80%**) for the corresponding boxplots and position on the dorsal view of each head shape. The horizonal grey bar represents no differences in torque production within each head shape. The colored letters above the dorsal view represents the HL% comparisons between head shapes with same letters meaning similarities (Tukey, $p > 0.05$) and different indicating differences between (Tukey, $p < 0.05$). The black letters represent the relationship between HL% within head shapes. Each boxplot represents five recordings.

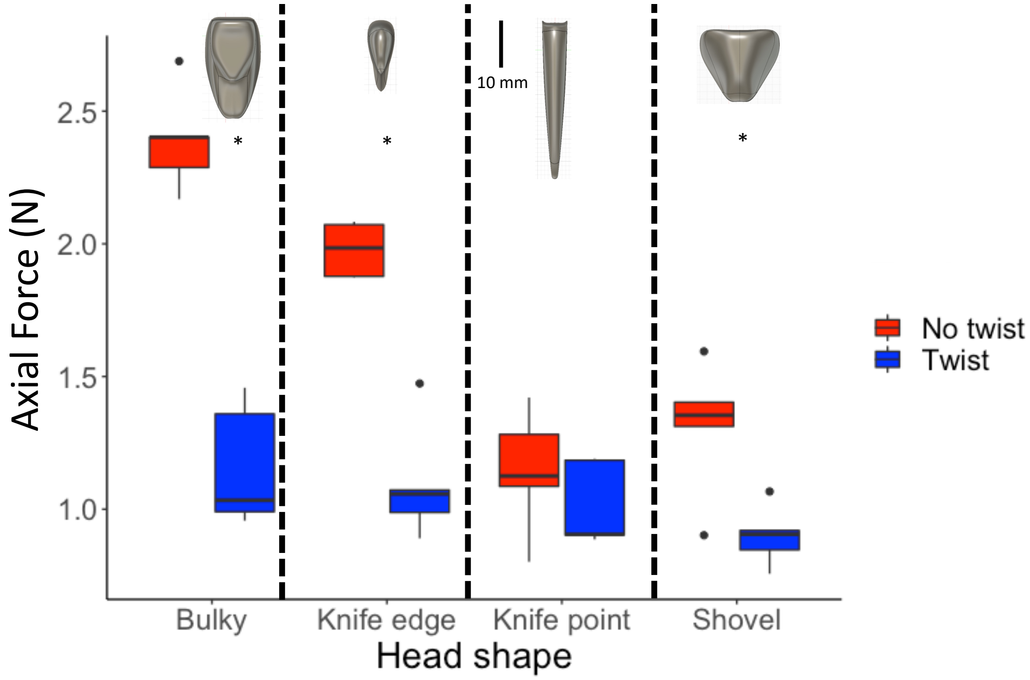

Figure 2.8: Axial force with torque versus no torque for each head shape. The **red** boxplots are axial forces recordings without torque, and **blue** boxplots are the recordings with torque. The vertical black dash lines separate the head shapes. The head shapes' dorsal view is above the boxplots. The asterisks (*) represent differences (Tukey, <0.05) between blue and red boxplots within head shapes. Each boxplot has five recordings.

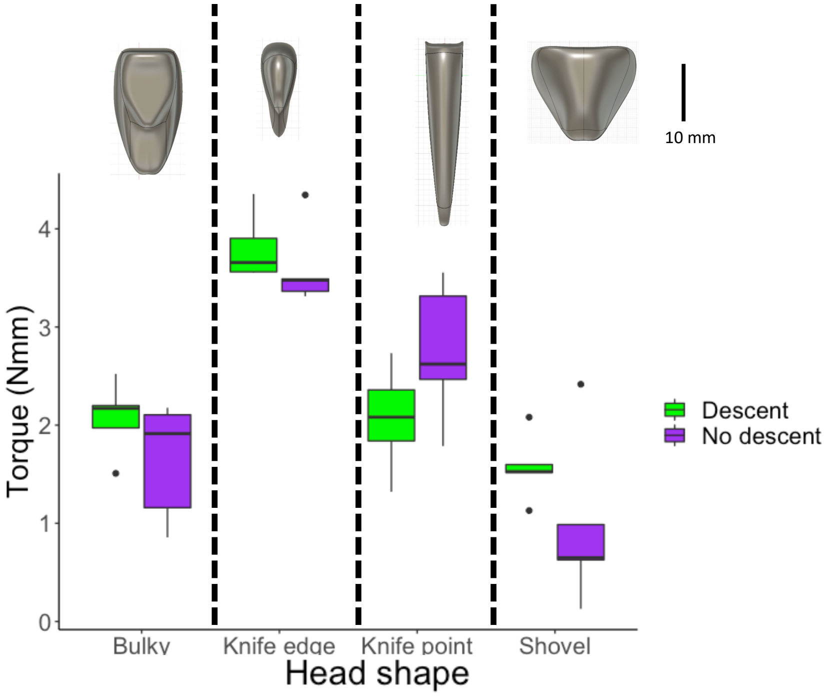

Figure 2.9: Torque production with descent and no descent for each head model. The **green** boxplots are torque recordings while descending, and **purple** boxplots are the recordings without descent or pausing. The vertical black dash lines separate the head shapes. The head shapes' dorsal view is above the boxplots. Each boxplot has five recordings.

2.6 Tables

Table 2.1: Maximum axial force (N) and torque (Nmm) of each specimen (Mean ± S.D). Below is the one-way ANOVA table with the main effects (head shape and percentage of burial depth) and interaction with respective p-values.

Head shape	Axial Force (N)	Torque (Nmm)
Bulky	2.32 ± 0.19	2.07 ± 0.37
Knife point	1.09 ± 0.23	2.06 ± 0.53
Knife edge	1.98 ± 0.10	3.80 ± 0.34
Shovel	1.55 ± 0.25	1.57 ± 0.34

ANOVA

	DF	Sum Sq	Mean Sq	F value	Pr(>F)	
Head shape (Axial)	3	1379837	459946	51.780	2e-16	***
Head shape ((Torque)	3	22.04	7.346	34.388	2.32e-13	***

Table 2.2: Torque (Nmm) (Mean ± S.D) with head percentages of all head shapes. Below is the two-way ANOVA table with main effects and interactions with their respective p-values.

	Torque (Nmm) (Mean ± SD)			
Head shape	**10%**	**30%**	**50%**	**80%**
Knife edge	0.578 ± 0.125	1.295 ± 0.440	2.064 ± 0.578	3.579 ± 1.136
Knife point	0.237 ± 0.091	0.805 ± 0.234	1.022 ± 0.356	1.536 ± 0.263
Bulky	0.835 ± 0.563	0.802 ± 0.435	0.704 ± 0.235	0.968 ± 0.687
Shovel	0.419 ± 0.287	0.480 ± 0.192	0.516 ± 0.317	0.430 ± 0.267

ANOVA

	DF	Sum Sq	Mean Sq	F value	Pr(>F)	
Head shape	3	22.04	7.346	34.388	2.32e-13	***
Percentage (Torque)	3	13.12	4.373	20.471	2.05e-09	***
Head shape: Percentage (Torque)	9	9	1.801	8.433	3.52e-08	***

Table 2.3: Axial forces (mN) (Mean ± S.D) with head percentages of all head shapes. Below is the two-way ANOVA table with main effects and interactions with their respective p-values.

	Axial Force (mN) (Mean ± SD)			
Head shape	**10%**	**30%**	**50%**	**80%**
Bulky	83.88 ± 31.55	357.71 ± 97.72	776.31 ± 163.20	1368. 83 ± 229.97
Knife point	72.94 ± 36.12	277.01 ± 125.34	644.50 ± 202.71	1201.72 ± 343.19
Knife edge	54.82 ± 26.35	218.39 ± 138.69	551.64 ± 247.44	1085.24 ± 376.62
Shovel	52.85 ± 27.63	194.05 ± 120.83	449.77 ± 270.24	1045.96 ± 388.22

ANOVA

	DF	Sum Sq	Mean Sq	F value	Pr(>F)	
Head shape	3	1379837	459946	51.780	2e-16	***
Percentage (Axial)	3	9290769	3096923	348.648	2e-16	***
Head shape: Percentage (Axial)	9	655982	72887	8.206	5.42e-08	***

Table 2.4: Axial (N) and torque (Nmm) force loading in isolation and combined. Upper table mean ± S.D; lower table, two-way ANOVA results for axial force production (head shape and twist) and torque (head shape and descent).

	Axial force (N)		Torque (Nmm)	
Head shape	**Twist**	**No twist**	**Descend**	**Pause**
Bulky	1.15 ± 0.10	2.32 ± 0.19	2.07 ± 0.37	1.64 ± 0.26
Knife point	1.01 ± 0.16	1.09 ± 0.24	2.06 ± 0.53	2.74 ± 0.71
Knife edge	1.09 ± 0.22	1.98 ± 0.10	3.80 ± 0.34	3.56 ± 0.42
Shovel	1.01 ± 0.16	1.55 ± 0.25	1.57 ± 0.34	1.12 ± 0.87

ANOVA

	DF	Sum Sq	Mean Sq	F value	Pr(>F)	
Head shape	3	2.694	0.898	18.03	4.94e-7	***
Twist	1	4.463	4.463	89.92	8.52e-11	***
Head shape: Twist	3	1.648	0.549	11.03	3.95e-5	***
Head shape	3	32.41	10.803	35.380	2.81e-10	***
Descent	1	0.201	0.201	0.659	0.4228	
Head shape: Descent	3	2.47	0.822	2.691	0.0627	

Table 2.5: The surface area (mm^2) and volume (mm^3) of the respective head length percentages (10, 30, 50, and 80%) for each model. All models had the same whole head surface area ($750mm^2$) with varying head volume.

	Surface Area (mm^2)				**Volume (mm^3)**				
	Percentage head length				Percentage head length				
Head shape	**10%**	**30%**	**50%**	**80%**	**10%**	**30%**	**50%**	**80%**	**100%**
Bulky	49.96	151.00	245.30	397.36	20.75	124.18	351	999.49	1504
Knife point	47.17	124.14	188.41	327.84	22.66	97.44	188.47	741.33	1130
Knife edge	114.98	230.91	309.96	426.85	56.60	156.89	256.31	968.24	1306
Shovel	66.82	240.33	254.89	416.50	29.67	139.31	229.08	920.56	1270

Table 2.6: The dimensions of 50% and 100% head length (HL) in height, width, and length (mm) of each model along with the respective Height:Width ratios. Note that a value of one is a perfectly cylindrical object, the larger or smaller the value the more plate-like the object.

	50% Head dimensions (mm)			**50% H:W**	**100% Head dimensions (mm)**			**100% H:W**
Head shape	Height	Width	Length	Height:Width	Height	Width	Length	Height:Width
Bulky	7	5	11	1.4	9	12	22	0.75
Knife point	6	5.5	16	1.09	6.8	7.1	32	0.95
Knife edge	19	4	8	4.75	14	5.5	16	2.55
Shovel	6	14	9	0.42	6.51	18.8	18	0.34

Chapter 3: Finite element analysis using 3D models of the neurocraniums to examine stress types and distributions.

3.1 Introduction

Head shape is an important factor for animals burrowing head-first that determines the sufficient force to burrow (Bergmann and Berry, 2021). The bony elements beneath the integument serve as a support frame and mitigate stress during burrowing (Cuff and Greaves, 1994; Dumont et al., 2005; Herrel et al., 2011; Rayfield, 2004). Bone is a dynamic tissue and can repair itself if fractured or damaged (Currey, 2002). It adjusts its' strength in response to the direction and magnitude of load it experiences. Bone performs better withstanding high compressive stresses, shortening the bone, as opposed to high tensile stresses, stretching the bone (Currey, 2002). During burrowing, the forces experienced by the skull bones are large and potentially damaging. There are several head shapes that are known to burrow. The goal of this paper is two-fold, first we are interested in understanding how stress is distributed across the different bones within a given skull shape and second, we want to see if there are differences in these patterns of stress concentration across differently shaped skulls.

A common method to observe stress distribution in an object is finite element analysis (FEA). Biologists use this technique to understand how stress concentrates in skeletal elements during animal behavior to gain insight into the selective pressures that act on an individual's morphology (Dumont et al., 2009; Rayfield, 2007; Ross, 2005). FEA reports the results in stress magnitudes (Pascals), which is the force (N) applied to an area (m^2) of a model that causes the model to deform or change its' shape. Minimizing high stress magnitudes avoids fracturing or cracking within the models under loading conditions. The maximum stress magnitude locations are the constraints upon the model. For example, FEA was used to examine the stress distributions of non-head-first and head-first burrowing eels' skulls and discovered that the head-first burrower's skull had a skull that was mechanically suitable for the head-first burrowing behavior by avoiding overwhelming stresses by distributing it throughout the skull (Herrel et al., 2011). This study hypothesized that the bones most susceptible to maximal stress during head-first burrowing were the premaxilla, maxilla, and frontal that compose their interorbital septum (De Schepper et al., 2007). They concluded that the greatest stress was experienced by the frontal bone, making it the limiting factor in overall burrowing performance (Herrel et al., 2011). Head morphology is specific in animals that burrow head-first. Obligate head-first burrowing eels have thicker and denser bones compared to non-head-first burrowers which presumably withstand high penetration forces (De Schepper et al., 2005; De Schepper et al., 2007). In addition, the number of fenestra in bones is believed to contribute to overall bone and skull strength as strategically placed voids in loaded bones actually help distribute stresses that could lead to cracking (Rayfield, 2004; Rayfield, 2011). Diet contributes to skull morphology where fish that crush are equipped with a robust skull to reduce cranial stresses (Cooper et al., 2011). Another tactic that reduces stresses on skulls during burrowing is fluidization of sediment during descent. Fluidization forces water into the sediment making it easier to get between particles and thus not requiring as robust skull morphology (Dorgan, 2015).

Although FEA is a powerful tool, very few studies look at the stress concentrations of differently shaped fish skulls that burrow. As mentioned above, Herrel et al 2011 discovered that the bones of the interorbital septum are important regions of stress concentration in eels. Interestingly, the bones that make up the skull of different head-first burrowers varies. How stress concentrations change across these different shapes and skeletal elements is of interest. All species in this study (Tetraodontiformes, Siluriformes and Labriformes) have a premaxilla, maxilla and frontal bone that make up the leading edge of the skull. In addition, the Labriformes and Tetraodontiformes are equipped with a parasphenoid which is a rod-like bone that runs ventral to the orbit and connects the ventral base of the cranium to the front of the skull (rostrum area) and forms some of interorbital septum (Fig. 3.1; 3.2). A previous study discovered that in fishes equipped with a parasphenoid (connecting the anterior bones to the neurocranium) that the parasphenoid experiences most of the load during feeding (Cooper et al., 2011). The parasphenoid in Teleosts serves as the origin of the abductor *arcus palatini* and adductor *hyomandibulae X* muscles (Atkins and Franz-Odendaal, 2015) which both compose the hyoid jaw muscles (Diogo et al., 2008). The parasphenoid has two functions 1) hyoid jaw muscle attachments and 2) taking the force loads during feeding.

There are limited studies examining the stress magnitudes and concentrations across different skull morphologies. The goal of this paper is to examine stress concentrations in different skull shapes. In addition, we will compare two similar skull shapes with different bone arrangements to elucidate a particular bone function. We hypothesize that these different fish skulls are designed to distribute and concentrate loads differently during a burial event. We predict that regardless of skull morphology, the force concentrations will be maximal in compression and minimal in tension due to bones optimal performance under compression. We also predict, given its location and orientation parallel to the longitudinal axis of the fish, that the parasphenoid bone will experience the greatest force loading during burial. Finally, when comparing two knife point head shapes with different bone arrangements, we predict that the skull with the parasphenoid will experience greater force concentrations in comparison with the skull without it.

3.2 Materials and Methods

3.2.1 Finite Element Analysis

Finite element analysis breaks the surface of an object into discrete areas and calculates possible stress concentrations within each area when the object is loaded. To conduct FEA, high resolution three-dimensional images are required of the shapes of interest. We used Blender version 2.93.4 (https://www.blender.org) a 3D image analysis software to model the different skull shapes (Fig. 3.3). Like how we modeled the head shapes for printing physical models for UTM testing (Chapter 2), we uploaded the neurocranium anterior, lateral, dorsal, and ventral views from 3DSlicer to Blender. Once the images were loaded and scaled on Blender, we used Blender's Sculpt mode for modeling the complete neurocranium, excluding the lower jaw, with emphasis on the premaxilla, maxilla, and frontal bone; in addition, the parasphenoid was modeled for bulky (*Tetraodon miurus)*, knife edge (*Iniistius pavo)*, and knife point (*Cheilio* *inermis)* (Fig. 3.3). From previous FEA related studies, we modeled the skulls as fused. After completing all sculpting and geometry scaling, we exported each skull as an STL file from Blender to conduct FEA. All blender models had uniform surface area (750 mm^2). We exported uniform surface area for all models because the interest of this study was examining the skull strength opposed to the skull strain energy, which is the energy requirements to deform the skull, that requires uniform volume for models (Dumont et al., 2009).

We loaded the STL files into ANSYS version 2022 R1 and conducted a static-structural analysis, which is a force applied to a solid and immobile model. We used a 10-noded tetrahedral as the element type and shape. The material assigned to all models was vertebrate bone (E = 20 GPa and 0.3 poisson ratio) (Erickson et al., 2002). We assigned bone as homogenous and isotropic even though this is unlikely (Currey, 2002). We assigned bone as the only material because there are limited studies examining the cartilaginous properties in bony fishes and lack of CT scans with stained cartilages. We applied a uniform load to all models that was one standard deviation over the pooled mean axial force across species recorded from UTM experimental data. The loads were applied axially, 90°, to the anterior side of each head shape. All models had the same scale loading conditions (equal force to surface area). The boundary condition was set at the foramen magnum for all models. The response variables were von Mises stress (a predictor of ductile material yield and failure under distortion and shear) in pascals (Pa) (Nalla et al., 2003), and principal directions of tensile and compressive stresses as vectors. Models were plotted on two separate scale bars to enable visual comparisons. First, on a single scale bar to visualize differences across all skull shapes, and second, on independent scale bars to enable visualization of differences between bones in each single skull shape. To ensure meshing was not affecting FEA results, we only refined the mesh size for the maximum stresses concentrated upon each model by reducing the mesh size. For each reduced mesh size, we ran average and unaverage von Mises stress simulations to compare the maximum stresses between. We ran simulations until maximum stress values had minuscule differences.

3.3 Results

3.3.1 von Mises stress patterns on loaded skulls

Comparing skull performances under burial loading, the knife point skull shape was the only shape with notable stress concentrations, and they occurred on the parasphenoid bone (Fig. 3.4). Bulky and knife edge shapes also had very slight stress concentrations on the parasphenoid. When comparing stress concentrations for each skull shape independently each shape had slightly different patterns. The shovel skull shape concentrated stresses on the posterior sides of the premaxillae and maxillae (0.96 MPa); moderate stresses were also present on the frontal bones and the ventral side of the skull (Fig. 3.5). The bulky skull shape had peaked von Mises stress (0.93 MPa) focused on the anteroventral half of the parasphenoid with more moderate stress distribution on the mid-posterior region of the parasphenoid and the frontal (Fig. 3.5). Knife point was like bulky but with much higher stress concentrations (2.54 MPa) on the anteroventral parasphenoid. For both the bulky and knifepoint skulls, there were minimal stress on the premaxillae, maxillae, and frontal bones. The knife edge skull shape also shown peak stresses on the anteroventral portion of the parasphenoid (0.63 MPa) as well as moderate stress concentrations on the frontal and premaxilla joint, but not on the maxilla (Fig. 3.5).

3.3.2 Compressive stresses versus tensile stresses on loaded skulls

Shovel skull shape had peak compressive stress occurring on the posterior of the premaxillae and maxillae with tensile stress loading on the anterior surface of these bones (Fig. 3.6). Additional compressive stress was felt along the ventral surface of the skull and tensile stress existed on dorsal side of the skull. In the bulky skull shape, the parasphenoid was dominated by compressive stress where peak stresses occurred on the anteroventral side of the parasphenoid (Fig. 3.6). The anteromedial tip of the bulky premaxilla also experienced compression while tensile stress was found on the frontal and some parts of the premaxilla. Knife point skull shape had peak compressive stress on the parasphenoid (Fig. 3.6). Although peak stresses were compressive, the parasphenoid and frontal bones of the knife point skull shape also experienced some tensile stress. The peak stress for the knife edge skull shape was compression on the parasphenoid (Fig. 3.6). The knife edge skull shape also experienced tensile stresses on the frontal, frontal-premaxilla joint, and posterior end of the neurocranium (Fig. 3.6).

3.4 Discussion

The purpose of this study was to understand if differences in skull shape impact how stress are concentrated in different skull bones during burial. Four different head shapes that are found in head-first burrowers were used in this study. Changes in stress concentration, as predicted by finite element analysis (FEA), will be discussed in the context of head shape, bone anatomy and phylogenetic constraint.

3.4.1 Effect of skull shape on stress magnitudes experienced during burrowing

Of the four different skull shapes, the FEA analysis of the knife point shape showed distinctly higher stress concentrations within the skull during loading (Fig. 3.4). Concentrations of stress on any skeletal element may damage or lead to failure of the bone, limiting animal burial performance. Although the higher stress concentrations experienced by the knife point shape could be considered detrimental to performance, the UTM experiments suggest that the overall axial forces that are experienced when this shape drives into the substrate are minimal. Potentially, the increase in stress concentrations may be mitigated by an overall lower force production associated with this skull shape during burial. In contrast, the higher forces experienced by the other skull shapes (bulky, knife edge and shovel) during burial as seen from the UTM study are distributed across the skulls and do not result in point concentrations of stress. This data suggests that selective pressure can act in multiple ways when determining burial performance. In the case of the knife point skull shape, selective pressure appears to be acting to reduce force production during burial while in the three other shapes, it appears to be selecting for bone geometry that distributes cranial stress produced during burrowing.

3.4.2 Bone arrangement and resultant stress concentration

Fish skulls can vary in their bone composition. In this study, bulky, knife edge, and knife point skull shapes all contain a parasphenoid bone (Fig 3.2). Interestingly, for each of these skull shapes, stress concentration during loading occurred on the parasphenoid but in slightly different ways (Fig. 3.5). For example, the parasphenoid for bulky and knife edge skull shapes experienced compressive loads only with bulky in a uniform distribution and knife edge in a more ventral position. In contrast, knifepoint had both compressive and tensile stresses concentrated on its' parasphenoid. These differences in force loading on similar bones confirms that bone geometry influences stress type and concentration across different skull shapes. The shovel skull shape lacks a parasphenoid (Fig. 3.2); maximal stress concentrations for this shape occurred on the posterior sides of the premaxillae and maxillae (Fig. 3.5). Because the parasphenoid (when present and connecting the anterior bones to the neurocranium) appears to bear the brunt of the stress concentration, it may play an important role to liberate stresses from other skull bones. With the presence of the parasphenoid (connecting the anterior bones to the neurocranium), it takes the load during burial, seen in our study, and in feeding (Cooper et al., 2011).

An interesting comparison can be made between two knife point skull shapes that have different stress concentration patterns during loading. The *Labridae* knife point (*C.inermis*) and Anguilliform knifepoint (*P.boro*) both have a knife point head shape with the same bones (premaxilla, maxilla, frontal, and parasphenoid), but in different arrangements (De Schepper et al., 2007; Fig. 3.1). As a result, stress concentrations are on different bones. In the Anguilliform knife point, maximum stress concentrates upon the frontal (Herrel et al. 2011), while the parasphenoid concentrates for the *Labridae* knifepoint. We know from our shovel shaped skull that the either the premaxillae, maxillae, or frontal bones absorbs the load when a parasphenoid is not present (Fig. 3.5). Although the parasphenoid is present in the Anguilliform knifepoint, the arrangement of skull bones is such that the anterior bones do not connect directly with the parasphenoid (Fig. 3.1; 3.2). In this way, stress concentrates on the frontal and not on the rather delicate paraspheoid in this species.

Force loading on bones determines their physiology, strength, and overall shape (Cooper et al., 2011; Currey, 2002; De Schepper at al., 2005; Rayfield, 2004; Standen et al., 2014). Thus, these slight differences in anatomy may be responsible for changes in force loading which in turn accentuates differences in anatomy (Currey, 2002; Dumont et al., 2009; Standen et al., 2014). Bone anatomy may have a role for withstanding forces, but the stress type influences bone performance (Currey, 2002). Bone performs best under compression (Currey, 2002), and the stress peak and concentration were compression for bulky, knife edge, and knife point skull shapes upon their parasphenoid (Fig. 3.6). Shovel skull shape yielded in compression in stress peak and concentration as well. Peak stress magnitudes and concentrations being dominated by compressive stress during the burial event could be favorable because bone realigns optimally under compressive loading (Currey, 2002). In the Anguilliform knife point skull shape, peak stress concentrations were compressive stresses as well (Herrel et al., 2011). Because all head shapes experienced peak stress magnitudes under compression, selection appears to be driven by the capacity of bone to resist compressive stresses resulting in morphology that experiences compressive loading during burial.

3.4.3 Cranial evolution within a family

It is also interesting to think about the evolution of head shape in burrowing. Within the *Labridae* family, knife point (*C.inermis)* is the ancestral head shape and knife edge (*I.pavo*) is the derived head shape (Tatom-Naecker and Westneat. 2018). It was hypothesized the *Xyrichtyinae* sub-family within the *Labridae*, which contains *I.pavo* and the other steep frontal profile head-first burrowing knife edge head shape members, were the specialize sub-family for this behavior (Videler, 1986). The change in skull geometry from knife point to knife edge impacts the overall stress concentration across the skull. For the knife point skull shape, there is some tension concentration on the parasphenoid. Bone has poor performance under tension (Curry, 2002) so the evolution of a knife edge skull shape that has a robust frontal bone and does not concentrate tensile stresses on the parasphenoid may be a selective advantage (Fig. 3.6). By moving tensile stresses to more robust skeletal features (frontal and dorsal roof bones in the knife edge skull shape) and keeping the delicate parasphenoid exposed to only compressive stresses, the parasphenoid may be protected from excessive tensile stresses (Fig. 3.6).

3.4.4 Conclusions

Skull shapes differed in burial performance with the same loading conditions where the knife point skull shape succumbed to maximal stress magnitudes. The parasphenoid was the bone that constrains burial for those equipped with one. The absence of the parasphenoid (shovel skull shape) or lacking the connection of the anterior bones to the neurocranium (Anguilliform knife point), either the premaxilla, maxilla, or frontal yields to maximal stress. The peak stress type for all four skull shapes was compressive stress which bone performs favorably, so selection may select compressive loading because bone can optimally reshape under compression loading. There is a cranial evolution shift within the *Labridae* family from the ancestral knife point skull shape to the derived knife edge skull shape. The knife point skull concentrated the higher stress loads and had both tensile and compressive stress occurring on the parasphenoid, compared to its' derived knife edge relative that distributed the stress loads throughout the skull and had tensile and compressive stress each appearing on the frontal and parasphenoid, respectively.

3.5 Figures

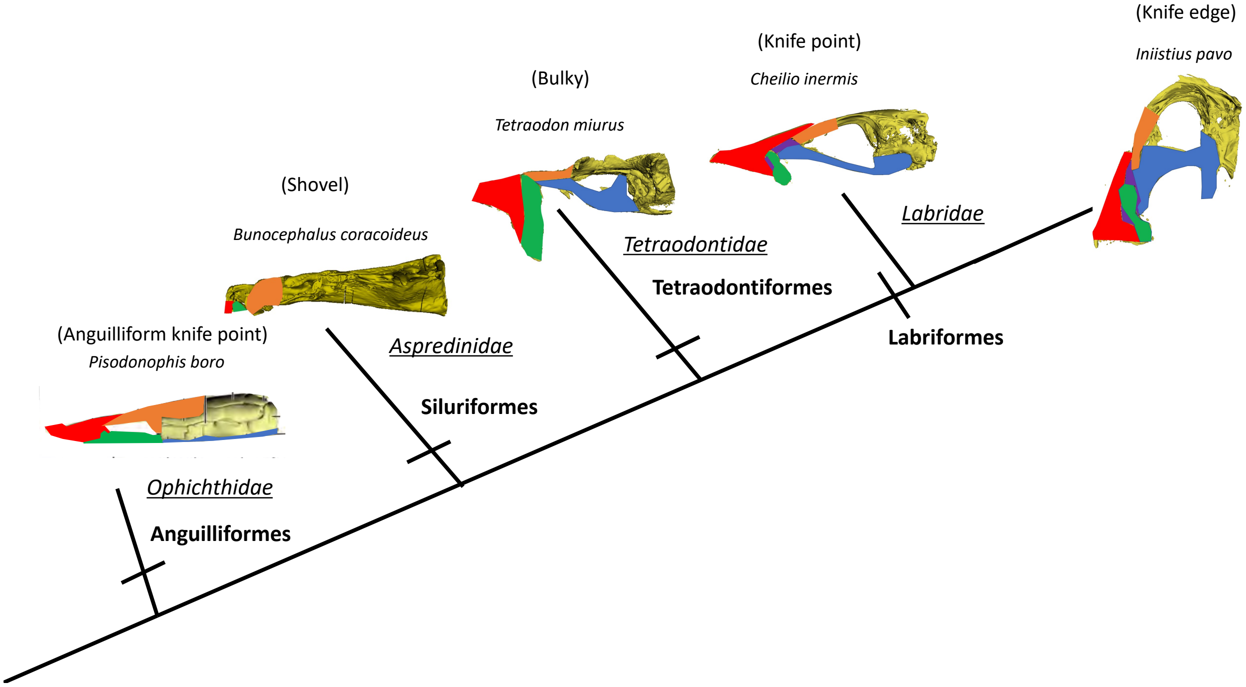

Figure 3.1: Phylogeny tree of burrowing fishes' skulls with color coded tissues. **Premaxilla**, **frontal**, and **maxilla** composing the interorbital septum observed in all fishes. The **parasphenoid** observed in the Anguilliformes, Tetraodontiformes, and Labriformes. Purple was a **cartilaginous** tissue. Images were obtained through 3DSlicer, but the image and bone names of *P.boro* were from De Schepper et al., 2007. Bone positions and names were color coded for knife edge (*I.pavo)* and knife point (*C.inermis)* from (Kousoulaki et al., 2021; Wainwright et al., 2004; Westneat et al., 2005), shovel (*B.coracoideus)* from (Carvalho and Reis, 2020), and bulky (*T.miurus)* from (Tyler and Patterson, 1991; Wainwright et al., 1995).

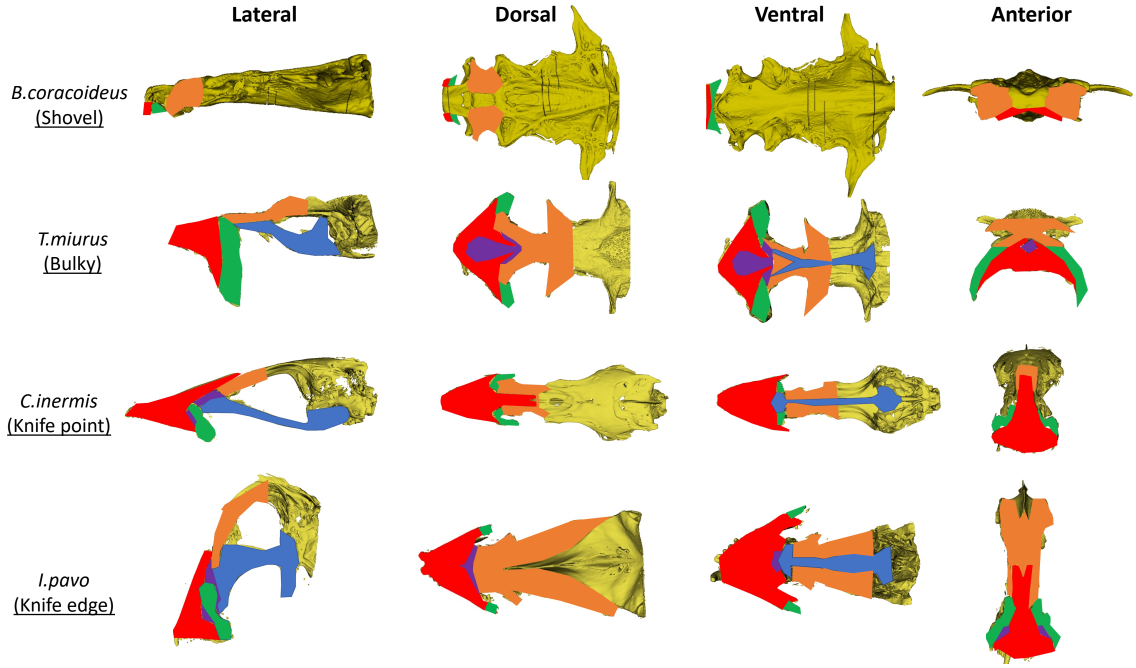

Figure 3.2: CT views of the studied specimens with their colored tissues. The coded color represents bones and tissues (**premaxilla**, **maxilla**, **frontal**, **parasphenoid**, and **cartilaginous** tissue). Images were obtained from 3D slicer. Bone positions and names were color coded for *I.pavo* and *C.inermis* from (Kousoulaki et al., 2021; Wainwright et al., 2004; Westneat et al., 2005), *B.coracoideus* from (Carvalho and Reis, 2020), and *T.miurus* from (Wainwright et al., 1995).

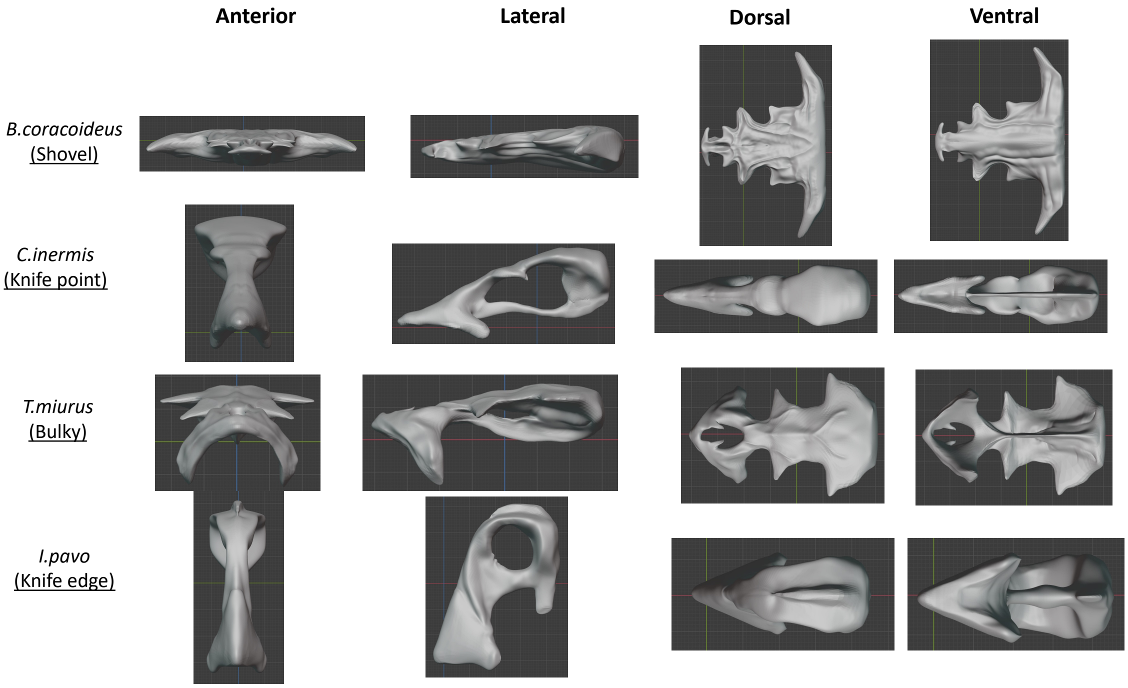

Figure 3.3: Four views of the blender models. Anterior, lateral, dorsal, and ventral views that were modeled in Blender by inserting 3Dslicer CT images.

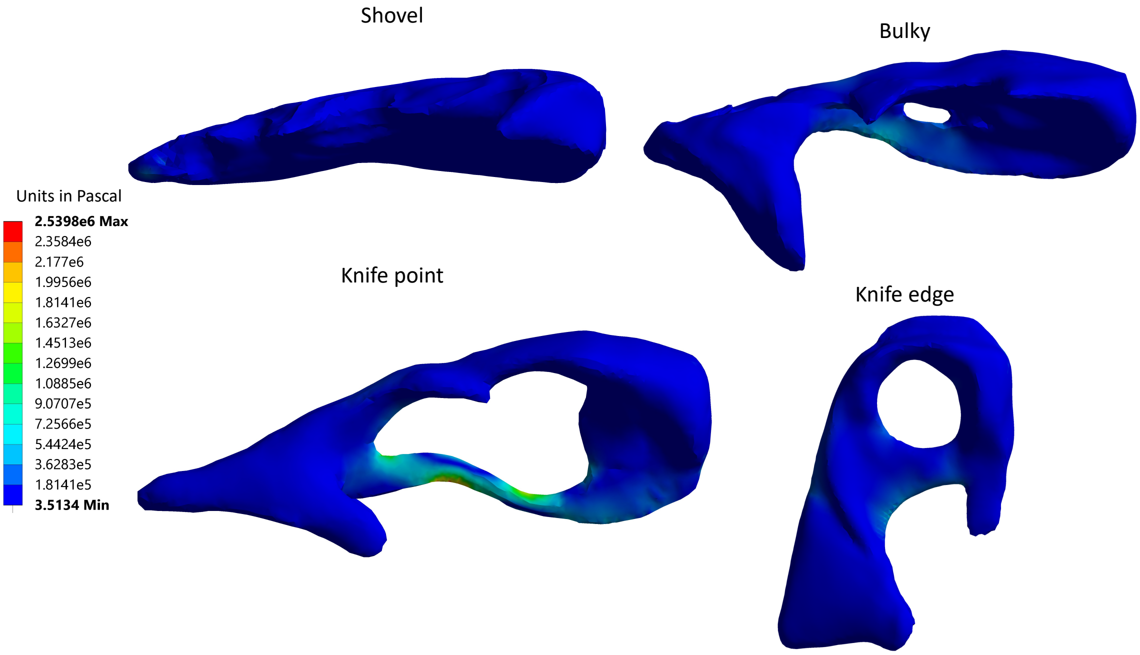

Figure 3.4: FEA models colored with uniform von Mises stress scales in units of Pascals. All models (shovel, bulky, knife point, and knife edge) were scaled to the same maximum and minimum stress. The head shapes are displayed in the lateral view with the appropriate name. Cooler colors are minimal stress to the minimum in **dark blue**. Warmer colors are higher stress to **red** being the maximum.

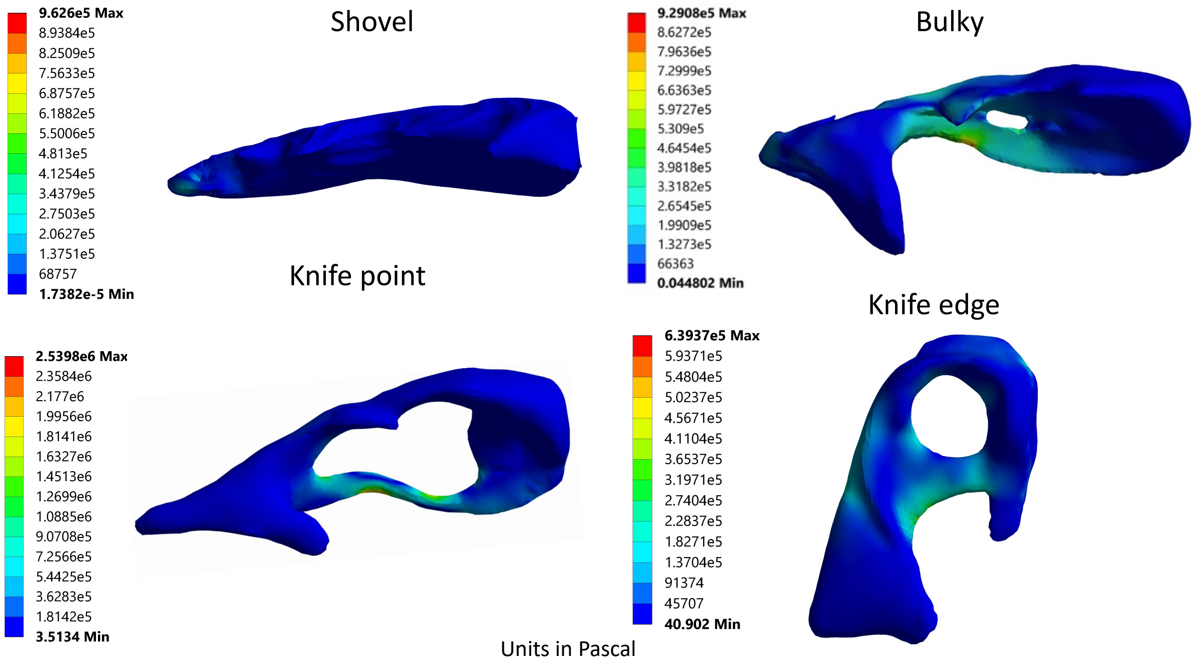

Figure 3.5: FEA models colored with their independent von Mises stress scales in units of Pascals. The lateral sides of shovel, bulky, knife point, and knife edge were displayed with their color scales at the left respectively. Cooler colors are minimal stress to **dark blue** being the minimum, and warmer colors are higher stresses with **red** being the maximum.

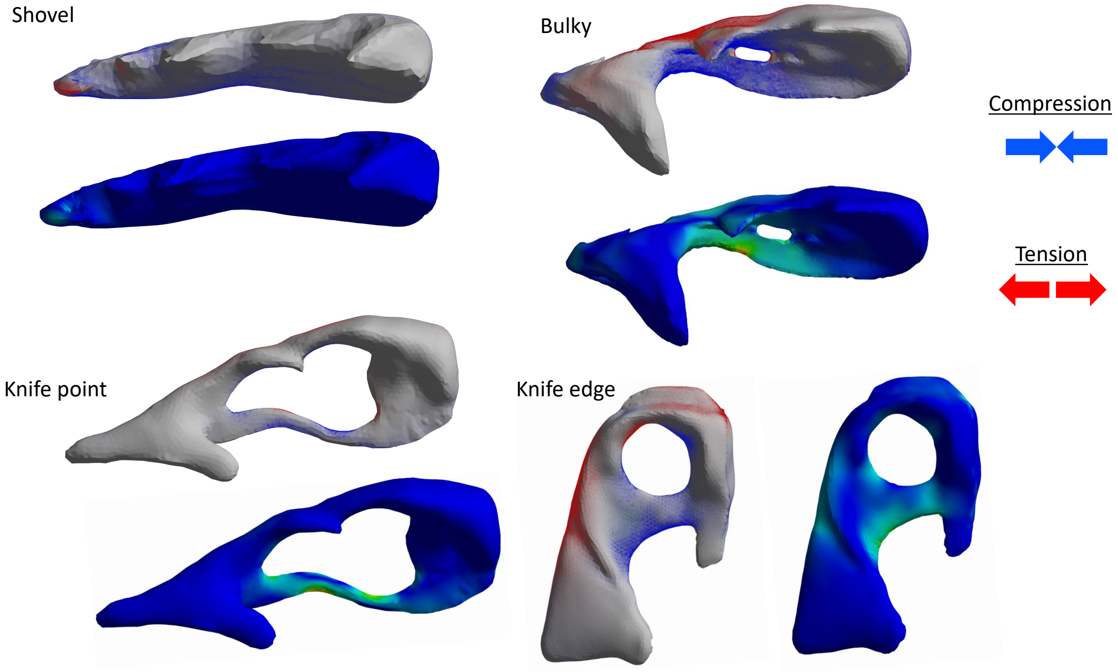

Figure 3.6: FEA models of principal directions of compressive and tensile stresses and von Mises within their independent stress scales. The grey models' lateral side shown with the principal directions displaying **compressive** and **tensile** stresses (arrows) simultaneously occurring for shovel (*B.coracoideus)*, bulky (*T.miurus)*, knife point (*C.inermis)*, and knife edge (*I.pavo)* models. The blue models are the same models from Fig. 3.5. Cooler colors are minimal stress to **dark blue** being the minimum, and warmer colors are higher stresses with **red** being the maximum for von Mises stress (Pa).

Chapter 4: Future studies

4.1 Future direction

Our results shown that two members from the *Labridae* family (the ancestral knife point, *C.inermis*, and derived knife edge, I.*pavo*) experienced two different axial forces and concentrated cranial stresses differently in magnitudes and principal directions when the same loading conditions were applied to their skulls. Although the knife point head shape experienced low axial force, the cranial stresses concentrated at high force magnitudes upon their parasphenoid within their skull and exhibited both tensile and compressive stress on the parasphenoid. In contrast, the knife edge head shape experienced more axial force, but its' skull distributed those forces compared to their ancestral relative. Like the knife point skull shape, the parasphenoid took the loading for the knife edge skull shape, but it was only compressive stress which bone performs optimally. This evolutionary shift from the *Labridae* ancestral skull where both tensile and compressive stresses occurring on the same bone and its' skull experiencing higher stress magnitudes to the *Labridae* derived skull with each compressive stress and tensile stress occurring on separate bones and distributing the loads through the skull could be a common trend amongst other head-first burrowing fish families. Thus, an interesting study will be looking at other head-first burrowing fish families between ancestral and derived members to determine if this trend is endemic to the *Labridae* family or a common trend for other families.

The force requirements to penetrate through the sediment varies depending on the granular media conditions where compacted conditions exponentiates the penetration force requirements and non-compacted conditions requires less penetration forces (Alexander et al., Bergmann and Berry, 2021; 1993; Sharpe et al., 2013; Sassa et al., 2011). The particle size and shape also influence force requirements where coarse particle sizes and angular shapes requires more penetration force than fine – medium particle sizes and spherical particle shapes (Alexander et al., 1993; Bergmann and Berry, 2021). When the granular media conditions are consistent, our study shown that different head shapes differ in penetration force requirements, and we know that the parasphenoid (if present and connecting the anterior bones to the neurocranium) took the load when applying the same burial load to their skulls. It is evident that the parasphenoid serves as the origin of the hyoid jaw muscles (Diogo et al., 2008), and it takes the force loads during burial seen in these specimens from our study and during feeding (Cooper et al., 2011). It will be an interesting study to raise head-first burrowing fish members in different sediment conditions and fed with different diets to determine if diets, sediment conditions, or both collectively reshapes bone morphology and performance under burial loads. This will address the phenotypic plasticity component that environmental changes can induce morphological changes in bone amongst head-first burrowing fishes (Muschick et al., 2011; Pigliucci et al., 2006; Standen et al., 2014).

When fish head-first burrow through a frictional fluid, they use a series of undulatory body movements (Gidmark et al., 2011; Tatom-Naecker and Westneat. 2018), but for penetrating through granular solids, it is hypothesized that they may adjust their burial strategy (Dorgan et al., 2007). Thus, it will be an interesting study to observe differences on their locomotory tactics when exposed to different sediment conditions. This will also determine which specimens are specialist, generalist, and sensitive. A specialist rapidly burrows in specific media conditions whereas a generalist burrows slowly in all media conditions (Alexander et al., 1993). Sensitive is defined as an individual that burrows rapidly in some media conditions and slowly in others (Alexander et al., 1993)

Appendix

Tukey comparisons and the adjusted p-values.

Isolated axial force

Head shape	Adjusted p-values
Knife edge-Bulky	0.0262143
Knife point-Bulky	0.0000002
Shovel-Bulky	0.0000017
Knife point-Knife edge	0.0000411
Shovel-Knife edge	0.0004967
Shovel-Knife point	0.5650879

Isolated torque production

Head shape	Adjusted p-values
Knife edge-Bulky	0.000024
Knife point-Bulky	0.9999892
Shovel-Bulky	0.2386359
Knife point-Knife edge	0.0000227
Shovel-Knife edge	0.0000009
Shovel-Knife point	0.2501601

Isolated Axial force with Head percentage

Head shape	Adjusted p-value
Knife edge-Bulky	0
Knife point-Bulky	0
Shovel-Bulky	0
Knife point-Knife edge	0.3320346
Shovel-Knife edge	0.704587
Shovel-Knife point	0.9243229

Head percentage	Adjusted p-value
30-10	0.0000011
50-10	0
80-10	0
50-30	0
80-30	0
80-50	0

Shape: Percentage	Adjusted p-value
Knife edge:10-Bulky:10	0.9993184
Knife point:10-Bulky:10	0.9999426
Shovel:10-Bulky:10	0.9999873
Bulky:30-Bulky:10	0.0020309
Knife edge:30-Bulky:10	0.7741391
Knife point:30-Bulky:10	1
Shovel:30-Bulky:10	0.7224004
Bulky:50-Bulky:10	0
Knife edge:50-Bulky:10	0.0000149
Knife point:50-Bulky:10	0.0140232
Shovel:50-Bulky:10	0.0006353
Bulky:80-Bulky:10	0
Knife edge:80-Bulky:10	0
Knife point:80-Bulky:10	0
Shovel:80-Bulky:10	0
Knife point:10-Knife edge:10	1
Shovel:10-Knife edge:10	1
Bulky:30-Knife edge:10	0.0000407
Knife edge:30-Knife edge:10	0.1433821
Knife point:30-Knife edge:10	0.9977622
Shovel:30-Knife edge:10	0.1180842

Bulky:50-Knife edge:10		0
Knife edge:50-Knife edge:10		0.0000002
Knife point:50-Knife edge:10		0.0003709
Shovel:50-Knife edge:10		0.0000113
Bulky:80-Knife edge:10		0
Knife edge:80-Knife edge:10		0
Knife point:80-Knife edge:10		0
Shovel:80-Knife edge:10		0
Shovel:10-Knife point:10		1
Bulky:30-Knife point:10		0.0000865
Knife edge:30-Knife point:10		0.2211381
Knife point:30-Knife point:10		0.9997198
Shovel:30-Knife point:10		0.1857092
Bulky:50-Knife point:10	0.0000000	0
Knife edge:50-Knife point:10		0.0000005
Knife point:50-Knife point:10		0.0007585
Shovel:50-Knife point:10		0.0000245
Bulky:80-Knife point:10		0
Knife edge:80-Knife point:10		0
Knife point:80-Knife point:10		0
Shovel:80-Knife point:10		0
Bulky:30-Shovel:10		0.0001243
Knife edge:30-Shovel:10		0.2682526
Knife point:30-Shovel:10		0.9999198
Shovel:30-Shovel:10		0.227595
Bulky:50-Shovel:10		0
Knife edge:50-Shovel:10		0.0000007
Knife point:50-Shovel:10		0.0010685
Shovel:50-Shovel:10		0.0000355
Bulky:80-Shovel:10		0
Knife edge:80-Shovel:10		0

Knife point:80-Shovel:10	0
Shovel:80-Shovel:10	0
Knife edge:30-Bulky:30	0.4693074
Knife point:30-Bulky:30	0.0030591
Shovel:30-Bulky:30	0.5269383
Bulky:50-Bulky:30	0.0000002
Knife edge:50-Bulky:30	0.992884
Knife point:50-Bulky:30	0.9999997
Shovel:50-Bulky:30	1
Bulky:80-Bulky:30	0
Knife edge:80-Bulky:30	0
Knife point:80-Bulky:30	0
Shovel:80-Bulky:30	0.0000022
Knife point:30-Knife edge:30	0.8407826
Shovel:30-Knife edge:30	0
Bulky:50-Knife edge:30	0
Knife edge:50-Knife edge:30	0.0218012
Knife point:50-Knife edge:30	0.8523614
Shovel:50-Knife edge:30	0.266921
Bulky:80-Knife edge:30	0
Knife edge:80-Knife edge:30	0
Knife point:80-Knife edge:30	0
Shovel:80-Knife edge:30	0
Shovel:30-Knife point:30	0.7962052
Bulky:50-Knife point:30	0
Knife edge:50-Knife point:30	0.0000237
Knife point:50-Knife point:30	0.020213
Shovel:50-Knife point:30	0.0009749
Bulky:80-Knife point:30	0
Knife edge:80-Knife point:30	0
Knife point:80-Knife point:30	0

Shovel:80-Knife point:30	0
Bulky:50-Shovel:30	0
Knife edge:50-Shovel:30	0.0278044
Knife point:50-Shovel:30	0.8893034
Shovel:50-Shovel:30	0.3118322
Bulky:80-Shovel:30	0
Knife edge:80-Shovel:30	0
Knife point:80-Shovel:30	0
Shovel:80-Shovel:30	0
Knife edge:50-Bulky:50	0.0000364
Knife point:50-Bulky:50	0
Shovel:50-Bulky:50	0.0000007
Bulky:80-Bulky:50	0
Knife edge:80-Bulky:50	0.9998985
Knife point:80-Bulky:50	0.9977188
Shovel:80-Bulky:50	0.9999995
Knife point:50-Knife edge:50	0.853296
Shovel:50-Knife edge:50	0.999692
Bulky:80-Knife edge:50	0
Knife edge:80-Knife edge:50	0.000001
Knife point:80-Knife edge:50	0.0000003
Shovel:80-Knife edge:50	0.0003613
Shovel:50-Knife point:50	0.9998857
Bulky:80-Knife point:50	0
Knife edge:80-Knife point:50	0
Knife point:80-Knife point:50	0
Shovel:80-Knife point:50	0.0000002
Bulky:80-Shovel:50	0
Knife edge:80-Shovel:50	0
Knife point:80-Shovel:50	0
Shovel:80-Shovel:50	0.0000081

Knife edge:80-Bulky:80	0
Knife point:80-Bulky:80	0
Shovel:80-Bulky:80	0
Knife point:80-Knife edge:80	1
Shovel:80-Knife edge:80	0.9744509
Shovel:80-Knife point:80	0.9032302

Torque production in head increments

Head shape	**Adjusted p-value**
Knife edge-Bulky	0
Knife point-Bulky	0.9603762
Shovel-Bulky	0.0690268
Knife point-Knife edge	0
Shovel-Knife edge	0
Shovel-Knife point	0.0198326

Head percentage	**Adjusted p-value**
30-10	0.1227646
50-10	0.0017178
80-10	0
50-30	0.401441
80-30	0.0000072
80-50	0.0018993

Shape: Percentage	**Adjusted p-value**
Knife edge:10-Bulky:10	0.999941
Knife point:10-Bulky:10	0.7904715
Shovel:10-Bulky:10	0.9870259

Bulky:30-Bulky:10	1
Knife edge:30-Bulky:10	0.9673394
Knife point:30-Bulky:10	1
Shovel:30-Bulky:10	0.9972994
Bulky:50-Bulky:10	1
Knife edge:50-Bulky:10	0.0075528
Knife point:50-Bulky:10	0.9999993
Shovel:50-Bulky:10	0.9991675
Bulky:80-Bulky:10	1
Knife edge:80-Bulky:10	0
Knife point:80-Bulky:10	0.5563837
Shovel:80-Bulky:10	0.9897989
Knife point:10-Knife edge:10	0.9982216
Shovel:10-Knife edge:10	1
Bulky:30-Knife edge:10	0.9999901
Knife edge:30-Knife edge:10	0.5187311
Knife point:30-Knife edge:10	0.9999879
Shovel:30-Knife edge:10	1
Bulky:50-Knife edge:10	1
Knife edge:50-Knife edge:10	0.0003711
Knife point:50-Knife edge:10	0.9778667
Shovel:50-Knife edge:10	1
Bulky:80-Knife edge:10	0.9931003
Knife edge:80-Knife edge:10	0
Knife point:80-Knife edge:10	0.1062302
Shovel:80-Knife edge:10	1
Shovel:10-Knife point:10	0.9999993
Bulky:30-Knife point:10	0.8510688
Knife edge:30-Knife point:10	0.0430368
Knife point:30-Knife point:10	0.8452888
Shovel:30-Knife point:10	0.9999703

Bulky:50-Knife point:10	0.963023
Knife edge:50-Knife point:10	0.0000043
Knife point:50-Knife point:10	0.3691049
Shovel:50-Knife point:10	0.9998334
Bulky:80-Knife point:10	0.4844438
Knife edge:80-Knife point:10	0
Knife point:80-Knife point:10	0.0034033
Shovel:80-Knife point:10	0.9999985
Bulky:30-Shovel:10	0.9942642
Knife edge:30-Shovel:10	0.2007457
Knife point:30-Shovel:10	0.9937202
Shovel:30-Shovel:10	1
Bulky:50-Shovel:10	0.9997884
Knife edge:50-Shovel:10	0.000049
Knife point:50-Shovel:10	0.7885283
Shovel:50-Shovel:10	1
Bulky:80-Shovel:10	0.8775536
Knife edge:80-Shovel:10	0
Knife point:80-Shovel:10	0.0244847
Shovel:80-Shovel:10	1
Knife edge:30-Bulky:30	0.9424649
Knife point:30-Bulky:30	1
Shovel:30-Bulky:30	0.9990848
Bulky:50-Bulky:30	1
Knife edge:50-Bulky:30	0.005226
Knife point:50-Bulky:30	0.9999931
Shovel:50-Bulky:30	0.9997703
Bulky:80-Bulky:30	0.9999998
Knife edge:80-Bulky:30	0
Knife point:80-Bulky:30	0.4768423
Shovel:80-Bulky:30	0.9956684

Knife point:30-Knife edge:30	0.9455253
Shovel:30-Knife edge:30	0.3012731
Bulky:50-Knife edge:30	0.803818
Knife edge:50-Knife edge:30	0.4002209
Knife point:50-Knife edge:30	0.9998493
Shovel:50-Knife edge:30	0.3739692
Bulky:80-Knife edge:30	0.9988964
Knife edge:80-Knife edge:30	0
Knife point:80-Knife edge:30	0.9999735
Shovel:80-Knife edge:30	0.2161473
Shovel:30-Knife point:30	0.9989678
Bulky:50-Knife point:30	1
Knife edge:50-Knife point:30	0.0054313
Knife point:50-Knife point:30	0.9999944
Shovel:50-Knife point:30	0.9997349
Bulky:80-Knife point:30	0.9999
Knife edge:80-Knife point:30	0
Knife point:80-Knife point:30	0.4849722
Shovel:80-Knife point:30	0.9952363
Bulky:50-Shovel:30	0.9999893
Knife edge:50-Shovel:30	0.0001062
Knife point:50-Shovel:30	0.8902436
Shovel:50-Shovel:30	1
Bulky:80-Shovel:30	0.9471972
Knife edge:80-Shovel:30	0
Knife point:80-Shovel:30	0.0439276
Shovel:80-Shovel:30	1
Knife edge:50-Bulky:50	0.0016962
Knife point:50-Bulky:50	0.9992941
Shovel:50-Bulky:50	0.999999
Bulky:80-Bulky:50	0.9999153

Knife edge:80-Bulky:50	0
Knife point:80-Bulky:50	0.2712747
Shovel:80-Bulky:50	0.9998651
Knife point:50-Knife edge:50	0.0492563
Shovel:50-Knife edge:50	0.0001679
Bulky:80-Knife edge:50	0.0301796
Knife edge:80-Knife edge:50	0.0002451
Knife point:80-Knife edge:50	0.9063487
Shovel:80-Knife edge:50	0.0000561
Shovel:50-Knife point:50	0.9331338
Bulky:80-Knife point:50	1
Knife edge:80-Knife point:50	0
Knife point:80-Knife point:50	0.9183311
Shovel:80-Knife point:50	0.8085847
Bulky:80-Shovel:50	0.9719185
Knife edge:80-Shovel:50	0
Knife point:80-Shovel:50	0.0612746
Shovel:80-Shovel:50	1
Knife edge:80-Bulky:80	0
Knife point:80-Bulky:80	0.8456674
Shovel:80-Bulky:80	0.8923054
Knife point:80-Knife edge:80	0.0000002
Shovel:80-Knife edge:80	0
Shovel:80-Knife point:80	0.0271496

Axial force with torque loading

Head shape	**Adjusted p-value**
Knife edge-Bulky	0.050267
Knife point-Bulky	0
Shovel-Bulky	0.0000001

Knife point-Knife edge	0.0000574
Shovel-Knife edge	0.0001427
Shovel-Knife point	0.9888468

Torque	**Adjusted p-value**
Twist -No twist	0.00E+00

Shape:Torque	**Adjusted p-value**
Knife edge:No twist-Bulky:No twist	0.0416003
Knife point:No twist-Bulky:No twist	0
Shovel:No twist-Bulky:No twist	0
Bulky:Twist -Bulky:No twist	0
Knife edge:Twist -Bulky:No twist	0
Knife point:Twist -Bulky:No twist	0
Shovel:Twist -Bulky:No twist	0
Knife point:No twist-Knife edge:No twist	0.0000034
Shovel:No twist-Knife edge:No twist	0.0001692
Bulky:Twist -Knife edge:No twist	0.000005
Knife edge:Twist -Knife edge:No twist	0.0000012
Knife point:Twist -Knife edge:No twist	0.0000002
Shovel:Twist -Knife edge:No twist	0
Shovel:No twist-Knife point:No twist	0.8636634
Bulky:Twist -Knife point:No twist	1
Knife edge:Twist -Knife point:No twist	0.9999345
Knife point:Twist -Knife point:No twist	0.963372
Shovel:Twist -Knife point:No twist	0.5173228
Bulky:Twist -Shovel:No twist	0.91391
Knife edge:Twist -Shovel:No twist	0.6567143
Knife point:Twist -Shovel:No twist	0.2683203
Shovel:Twist -Shovel:No twist	0.0395707
Knife edge:Twist -Bulky:Twist	0.9995207

Knife point:Twist -Bulky:Twist	0.9326983
Shovel:Twist -Bulky:Twist	0.4360558
Knife point:Twist -Knife edge:Twist	0.9973489
Shovel:Twist -Knife edge:Twist	0.7526601
Shovel:Twist -Knife point:Twist	0.9814237

Torque with axial loading

Head shape	**Adjusted p-value**
Knife edge-Bulky	0.0000001
Knife point-Bulky	0.1385525
Shovel-Bulky	0.098031
Knife point-Knife edge	0.0000569
Shovel-Knife edge	0
Shovel-Knife point	0.0003332

Descent	**Adjusted p-value**
No descent-Descent	4.23E-01

Shape:Descent	**Adjusted p-value**
Knife edge:Descent-Bulky:Descent	5.40E-04
Knife point:Descent-Bulky:Descent	1.00E+00
Shovel:Descent-Bulky:Descent	8.31E-01
Bulky:No descent-Bulky:Descent	9.14E-01
Knife edge:No descent-Bulky:Descent	2.85E-03
Knife point:No descent-Bulky:Descent	0.5417027
Shovel:No descent-Bulky:Descent	0.056732
Knife point:Descent-Knife edge:Descent	0.0005069
Shovel:Descent-Knife edge:Descent	0.0000089
Bulky:No descent-Knife edge:Descent	0.0000159
Knife edge:No descent-Knife edge:Descent	0.9986759
Knife point:No descent-Knife edge:Descent	0.0810742

Shovel:No descent-Knife edge:Descent	0.0000001
Shovel:Descent-Knife point:Descent	0.8413698
Bulky:No descent-Knife point:Descent	0.9215795
Knife edge:No descent-Knife point:Descent	0.0026797
Knife point:No descent-Knife point:Descent	0.5275045
Shovel:No descent-Knife point:Descent	0.0597077
Bulky:No descent-Shovel:Descent	0.999999
Knife edge:No descent-Shovel:Descent	0.0000487
Knife point:No descent-Shovel:Descent	0.0365372
Shovel:No descent-Shovel:Descent	0.6610215
Knife edge:No descent-Bulky:No descent	0.0000875
Knife point:No descent-Bulky:No descent	0.0590693
Shovel:No descent-Bulky:No descent	0.5304916
Knife point:No descent-Knife edge:No descent	0.2626278
Shovel:No descent-Knife edge:No descent	0.0000004
Shovel:No descent-Knife point:No descent	0.0003441

References

Able, K. W., Grimes, C. B., Cooper, R. A., & Uzmann, J. R. (1982). Burrow construction and behavior of tilefish, Lopholatilus chamaeleonticeps, in Hudson Submarine Canyon. *Environmental Biology of Fishes*, *7*(3), 199–205. https://doi.org/10.1007/BF00002496

Albert, I., Tegzes, P., Kahng, B., Albert, R., Sample, J. G., Pfeifer, M., Barabási, A. L., Vicsek, T., & Schiffer, P. (2000). Jamming and Fluctuations in Granular Drag. *Physical Review Letters*, *84*(22), 5122. https://doi.org/10.1103/PhysRevLett.84.5122

Albert, R., Pfeifer, M. A., Barabási, A. L., & Schiffer, P. (1999). Slow drag in a granular medium. *Physical Review Letters*, *82*(1), 205–208. https://doi.org/10.1103/PhysRevLett.82.205

Alexander, R. R., Stanton, R. J., & Dodd, J. R. (1993). Influence of sediment grain size on the burrowing of bivalves: correlation with distribution and stratigraphic persistence of selected Neogene clams. *Palaios*, *8*(3), 289–303. https://doi.org/10.2307/3515151

Atkins, J. B., & Franz-Odendaal, T. A. (2016). The evolutionary and morphological history of the parasphenoid bone in vertebrates. *Acta Zoologica*, *97*(2), 255–263. https://doi.org/10.1111/azo.12131

Benesch, A. R., & Withers, P. C. (2002). Burrowing performance and the role of limb reduction in Lerista (Scincidae, Lacertilia). *Senckenbergiana Lethaea*, *82*(1), 107–114. https://doi.org/10.1007/BF03043776/METRICS

Bergmann, P. J., & Berry, D. S. (2021). How head shape and substrate particle size affect fossorial locomotion in lizards. *Journal of Experimental Biology*, *224*(11). https://doi.org/10.1242/JEB.242244

Biewener, A. A. and Patek, S. N. (2018). Animal Locomotion, 2nd edn, pp. 90-95. Oxford University Press

Bilecenoğlu, M. (2005). Observations on the burrowing behaviour of the dwarf blaasop, torquigener flavimaculosus (osteichthyes: Tetraodontidae) along the coast of fethiye, turkey. *Zoology in the Middle East*, *35*(1), 29–34. https://doi.org/10.1080/09397140.2005.10638100

Bizzarro, J. J., Peterson, A. N., Blaine, J. M., Balaban, J. P., Greene, H. G., & Summers, A. P. (2016). Burrowing behavior, habitat, and functional morphology of the pacific sand lance (Ammodytes personatus). *Fishery Bulletin*, *114*(4), 445–460. https://doi.org/10.7755/FB.114.4.7

Bovy, J., Murray, I., Hogg, D. W., Du, W., Wang, D., Zhou, Y., Clark, A. H., & Behringer, R. P. (2013). Granular impact model as an energy-depth relation. *Europhysics Letters*, *101*(6), 64001. https://doi.org/10.1209/0295-5075/101/64001

Brainerd, E. L. (1994). Pufferfish inflation: Functional morphology of postcranial structures in Diodon holocanthus (Tetraodontiformes). *Journal of Morphology*, *220*(3), 243–261. https://doi.org/10.1002/JMOR.1052200304

Broek, D., & Rice, J. R. (1975). Elementary Engineering Fracture Mechanics. In *Journal of Applied Mechanics* (Vol. 42, Issue 3, pp. 751–752). https://doi.org/10.1115/1.3423697

Brzinski, T. A., Mayor, P., & Durian, D. J. (2013). Depth-dependent resistance of granular media to vertical penetration. *Physical Review Letters*, *111*(16), 168002. https://doi.org/10.1103/PHYSREVLETT.111.168002/FIGURES/3/MEDIUM

Buser, T. J., Sidlauskas, B. L., & Summers, A. P. (2018). 2D or Not 2D? Testing the Utility of 2D Vs. 3D Landmark Data in Geometric Morphometrics of the Sculpin Subfamily Oligocottinae (Pisces; Cottoidea). *Anatomical Record*, *301*(5), 806–818. https://doi.org/10.1002/ar.23752

C.E.Brennen. (1982). A review of added mass and fluid inertial forces. *Ocean Engineering*, *January*. https://authors.library.caltech.edu/233/

Carlson, K.J. (1968). *The Skull Morphology and Estivation Burrows of the Permian Lungfish , Gnathorhiza Serrata Author (s): Keith J . Carlson Source : The Journal of Geology , Nov ., 1968 , Vol . 76 , No . 6 (Nov ., 1968), pp . 641-663 Published by : The University of Chic*. *76*(6), 641–663.

Carvalho, M. S., Zuanon, J., & Ferreira, E. J. G. (2014). Diving in the sand: The natural history of Pygidianops amphioxus (Siluriformes: Trichomycteridae), a miniature catfish of Central Amazonian streams in Brazil. Environmental Biology of Fishes, 97(1), 59–68. https://doi.org/10.1007/s10641-013-0123-9

Cooper, W. J., Wernle, J., Mann, K., & Albertson, R. C. (2011). Functional and Genetic Integration in the Skulls of Lake Malawi Cichlids. *Evolutionary Biology*, *38*(3), 316–334. https://doi.org/10.1007/S11692-011-9124-9/TABLES/2

Covey, D. S. G., & Greaves, W. S. (1994). Jaw dimensions and torsion resistance during canine biting in the Carnivora. Canadian Journal of Zoology, 72(6), 1055–1060. https://doi.org/10.1139

Cuff, A. R., & Rayfield, E. J. (2013). Feeding Mechanics in Spinosaurid Theropods and Extant Crocodilians. *PLoS ONE*, *8*(5), 1–11. https://doi.org/10.1371/journal.pone.0065295

Currey, J. D. (2002). Bones: Structure and Mechanics. Princeton University Press. http://www.jstor.org/stable/j.ctt4cg9wv

De Schepper, N., Adriaens, D., & De Kegel, B. (2005). Moringua edwardsi (Moringuidae: Anguilliformes): Cranial specialization for head-first burrowing? *Journal of Morphology*, *266*(3), 356–368. https://doi.org/10.1002/jmor.10383

De Schepper, N., De Kegel, B., & Adriaens, D. (2007). *Pisodonophis boro* (Ophichthidae: Anguilliformes): Specialization for head-first and tail-first burrowing? Journal of Morphology, 268(2), 112–126. https://doi.org/10.1002/jmor.10507

Ding, Y., Sharpe, S. S., Masse, A., & Goldman, D. I. (2012). Mechanics of Undulatory Swimming in a Frictional Fluid. *PLOS Computational Biology*, *8*(12), e1002810. https://doi.org/10.1371/JOURNAL.PCBI.1002810

Diogo, R., Hinits, Y., & Hughes, S. M. (2008). Development of mandibular, hyoid and hypobranchial muscles in the zebrafish: homologies and evolution of these muscles within bony fishes and tetrapods. *BMC Developmental Biology*, *8*, 24. https://doi.org/10.1186/1471-213X-8-24

Diogo, R., Hinits, Y., & Hughes, S. M. (2008). Development of mandibular, hyoid and hypobranchial muscles in the zebrafish: homologies and evolution of these muscles within bony fishes and tetrapods. BMC Developmental Biology, 8, 24. https://doi.org/10.1186/1471-213X-8-24

Dorgan, K. M. (2015). The biomechanics of burrowing and boring. *Journal of Experimental Biology*, *218*(2), 176–183. https://doi.org/10.1242/jeb.086983

Dorgan, K. M., Arwade, S. R., & Jumars, P. A. (2007). Burrowing in marine muds by crack propagation: kinematics and forces. *Journal of Experimental Biology*, *210*(23), 4198–4212. https://doi.org/10.1242/JEB.010371

Dorgan, K. M., Jumars, P. A., Johnson, B., Boudreau, B. P., & Landis, E. (2005). Burrow extension by crack propagation. *Nature*, *433*(7025), 475. https://doi.org/10.1038/433475a

Ducey, P. K., Formanowicz, D. R., Boyet, L., Mailloux, J. and Nussbaum, R. A. (1993). Experimental examination of burrowing behavior in caecilians (Amphibia: Gymnophiona): Effects of soil compaction on burrowing ability in four species. Herpetologica 49, 450-457

Dumont, E. R., Grosse, I. R., & Slater, G. J. (2009). Requirements for comparing the performance of finite element models of biological structures. Journal of Theoretical Biology, 256(1), 96–103. https://doi.org/10.1016/j.jtbi.2008.08.017

Dumont, E. R., Piccirillo, J., & Grosse, I. R. (2005). Finite-element analysis of biting behavior and bone stress in the facial skeletons of bats. Anatomical Record - Part A Discoveries in Molecular,

Erickson, G. M., Catanese Iii, J., & Keaveny, T. M. (2002). Evolution of the Biomechanical Material Properties of the Femur. Anat Rec, 268, 115–124. https://doi.org/10.1002/ar.10145

Franzini, J. B., Finnemore, E. J., & Daugherty, R. L. (1997). *Fluid mechanics with engineering applications*. New York: McGraw-Hill

Gidmark, N. J., Pos, K., Matheson, B., Ponce, E., Westneat, M. W., Gidmark, N. J., Pos, · K, Matheson, · B, Ponce, · E, & Westneat, · M W. (2019). *Functional Morphology and Biomechanics of Feeding in Fishes*. 297–332. https://doi.org/10.1007/978-3-030-13739-7_9

Gidmark, N. J., Strother, J. A., Horton, J. M., Summers, A. P., & Brainerd, E. L. (2011). Locomotory transition from water to sand and its effects on undulatory kinematics in sand lances (Ammodytidae). *Journal of Experimental Biology*. https://doi.org/10.1242/jeb.047068

Goldman, D. I., & Umbanhowar, P. (2008). Scaling and dynamics of sphere and disk impact into granular media. *Physical Review E - Statistical, Nonlinear, and Soft Matter Physics*, *77*(2), 021308. https://doi.org/10.1103/PHYSREVE.77.021308/FIGURES/22/MEDIUM

Herrel, A., Choi, H. F., Dumont, E., Schepper, N. De, Vanhooydonck, B., Aerts, P., & Adriaens, D. (2011). Burrowing and subsurface locomotion in anguilliform fish: Behavioral specializations and mechanical constraints. *Journal of Experimental Biology*, *214*(8), 1379–1385. https://doi.org/10.1242/jeb.051185

Hosoi, A. E., & Goldman, D. I. (2015). Beneath Our Feet: Strategies for Locomotion in Granular Media. *Https://Doi.Org/10.1146/Annurev-Fluid-010313-141324*, *47*, 431–453. https://doi.org/10.1146/ANNUREV-FLUID-010313-141324

Katsuragi, H., & Durian, D. J. (2013). Drag force scaling for penetration into granular media. *Physical Review E - Statistical, Nonlinear, and Soft Matter Physics*, *87*(5), 2–6. https://doi.org/10.1103/PhysRevE.87.052208

Kousoulaki, K., Grøtan, E., Kortner, T. M., Berge, G. M., Haustveit, G., Krogdahl, Nygaard, H., Sæle, Chikwati, E. M., & Lein, I. (2021). Technical feed quality influences health, digestion patterns, body mineralization and bone development in farming of the stomachless cleaner fish ballan wrasse (Labrus bergylta). Animal Feed Science and Technology, 274(February). https://doi.org/10.1016/j.anifeedsci.2021.114830

Le Bail, P.-Y., Keith, P., & Planquette, P. (2000). *Atlas of freshwater fished of Guyana: Siluriformes*. *43*(2), 307.

Lewis, D. B. (1976). Studies of the biology of the lesser weever fish Trachinus vipera Cuvier: I. Adaptations to a benthic habit. *Journal of Fish Biology*, *8*(2), 127–138. https://doi.org/10.1111/j.1095-8649.1976.tb03926.x

Lin, Y. F., Konow, N., & Dumont, E. R. (2019). How moles destroy your lawn: The forelimb kinematics of eastern moles in loose and compact substrates. *Journal of Experimental Biology*, *222*(4). https://doi.org/10.1242/jeb.182436

Maladen, R. D. (2009). *Undulatory Swimming in Sand : 314*(July), 314–319. https://doi.org/10.1126/science.1172490

Maladen, R. D., Ding, Y., Umbanhowar, P. B., Kamor, A., & Goldman, D. I. (2011). Mechanical models of sandfish locomotion reveal principles of high performance subsurface sand-swimming. *Journal of the Royal Society, Interface*, *8*(62), 1332–1345. https://doi.org/10.1098/RSIF.2010.0678

McKee, A., MacDonald, I., Farina, S. C., & Summers, A. P. (2016). Undulation frequency affects burial performance in living and model flatfishes. *Zoology*. https://doi.org/10.1016/j.zool.2015.12.004

Meysman, F. J. R., Middelburg, J. J., & Heip, C. H. R. (2006). Bioturbation: a fresh look at Darwin's last idea. *Trends in Ecology and Evolution*, *21*(12), 688–695. https://doi.org/10.1016/j.tree.2006.08.002

Muschick, M., Barluenga, M., Salzburger, W., & Meyer, A. (2011). Adaptive phenotypic plasticity in the Midas Cichlid fish pharyngeal jaw and its relevance in adaptive radiation. *BMC Evolutionary Biology*, *11*(1), 116. https://doi.org/10.1186/1471-2148-11-116

Nalla, R. K., Kinney, J. H., & Ritchie, R. O. (2003). Mechanistic fracture criteria for the failure of human cortical bone. Nature Materials, 2(3), 164–168. https://doi.org/10.1038/NMAT832<

Pigliucci, M., Murren, C. J., & Schlichting, C. D. (2006). Phenotypic plasticity and evolution by genetic assimilation. *Journal of Experimental Biology*, *209*(12), 2362–2367. https://doi.org/10.1242/jeb.02070

Pradhan, N. R., Ph, D., & Army, U. S. (n.d.). *Newtonian and Non-Newtonian sediment fluid flow hydrodynamic runoff model*.

Rayfield, E. J. (2004). Cranial mechanics and feeding in Tyrannosaurus rex. Proceedings of the Royal Society B: Biological Sciences, 271(1547), 1451–1459. https://doi.org/10.1098/rspb.2004.2755

Rayfield, E. J. (2007). Finite element analysis and understanding the biomechanics and evolution of living and fossil organisms. Annual Review of Earth and Planetary Sciences, 35, 541–576. https://doi.org/10.1146/annurev.earth.35.031306.140104

Rayfield, E. J. (2011). Structural performance of tetanuran theropod skulls, with emphasis on the Megalosauridae, Spinosauridae and Carcharodontosauridae. Special Papers in Palaeontology, 86, 241–253. https://doi.org/10.1111/j.1475-4983.2011.01081.x

Roberts, T. R. (2015). Mimicry of a Bean Seed by the Amazonian Aspredinid Catfish Amaralia hypsiura (Kner 1855), with Notes on Vegetative Camouflage by Fishes. *Aqua, International Journal of Ichthyology*, *21*(3), 120–127.

Ross, C. F. (2005). Finite element analysis in vertebrate biomechanics. The Anatomical Record Part A: Discoveries in Molecular, Cellular, and Evolutionary Biology, 283A(2), 253–258. https://doi

Sassa, S., Watabe, Y., Yang, S., & Kuwae, T. (2011). Burrowing criteria and burrowing mode adjustment in bivalves to varying geoenvironmental conditions in intertidal flats and beaches. *PLoS ONE*, *6*(9). https://doi.org/10.1371/journal.pone.0025041

Sfakiotakis, M., Lane, D. M., & Davies, J. B. C. (1999). Review of fish swimming modes for aquatic locomotion. *IEEE Journal of Oceanic Engineering*, *24*(2), 237–252. https://doi.org/10.1109/48.757275

Sharpe, S. S., Ding, Y., & Goldman, D. I. (2013). Environmental interaction influences muscle activation strategy during sand-swimming in the sandfish lizard Scincus scincus. *Journal of Experimental Biology*, *216*(2), 260–274. https://doi.org/10.1242/JEB.070482

Standen, E. M., Du, T. Y., & Larsson, H. C. E. (2014). Developmental plasticity and the origin of tetrapods. *Nature*, *513*(7516), 54–58. https://doi.org/10.1038/nature13708

Steendam, C., Verhelst, P., Van Wassenbergh, S., & De Meyer, J. (2020). Burrowing behaviour of the European eel (Anguilla anguilla): Effects of life stage. *Journal of Fish Biology*, *97*(5), 1332–1342. https://doi.org/10.1111/jfb.14481

Stone, M. B., Barry, R., Bernstein, D. P., Pelc, M. D., Tsui, Y. K., & Schiffer, P. (2004). Local jamming via penetration of a granular medium. *Physical Review E - Statistical Physics, Plasmas, Fluids, and Related Interdisciplinary Topics*, *70*(4), 10. https://doi.org/10.1103/PhysRevE.70.041301

Stoner, A. W., & Ottmar, M. L. (2003). Relationships between size-specific sediment preferences and burial capabilities in juveniles of two Alaska flatfishes. *Journal of Experimental Marine Biology and Ecology*. https://doi.org/10.1016/S0022-0981(02)00447-1

Tatom-Naecker, T. A. M., & Westneat, M. W. (2018). Burrowing fishes: Kinematics, morphology and phylogeny of sand-diving wrasses (Labridae). *Journal of Fish Biology*. https://doi.org/10.1111/jfb.13789

Tyler, J. C., & Patterson, C. (1991). The Skull Of The Eocene Triodon antiquus (Triodontidae, Tetraodontiformes) - Similar To That Of The Recent Threetooth Pufferfish T-Macropterus. Proceedings of The Biological Society of Washington, 104, 878–891.

Videler, J. J. (1986). Sleep under sand cover of the labrid fish Coris julis. *Phylogeny of Sleep*, *May*, 145–147.

Wainwright, P. C., Bellwood, D. R., Westneat, M. W., Grubich, J. R., & Hoey, A. S. (2004). A functional morphospace for the skull of labrid fishes: Patterns of diversity in a complex biomechanical system. Biological Journal of the Linnean Society, 82(1), 1–25. https://doi.org/10.1111/j.1095-8312.2004.00313.x

Wainwright, P. C., Turingan, R. G., Brainerd, E. L., Wainwright, P. C., Turingan, R. G., & Brainerd, E. L. (1995). Functional Morphology of Pufferfish Inflation : Mechanism of the Buccal Pump Published by : American Society of Ichthyologists and Herpetologists (ASIH) Stable URL : http://www.jstor.org/stable/1446758 Functional Morphology of Pufferfish Inflation : Mec. Copeia, 3(3), 614–625.

Webb, P. W. (1984). Form and Function in Fish Swimming. *Scientific American*, *251*(1), 72–82. https://doi.org/10.1038/scientificamerican0784-72

Westneat, M. W., Alfaro, M. E., Wainwright, P. C., Bellwood, D. R., Grubich, J. R., Fessler, J. L., Clements, K. D., & Smith, L. L. (2005). Local phylogenetic divergence and global evolutionary convergence of skull function in reef fishes of the family Labridae. Proceedings of the Royal Society B: Biological Sciences, 272(1567), 993–1000. https://doi.org/10.1098/rspb.2004.3013

Young, B. A., & Morain, M. (2003). Vertical burrowing in the Saharan sand vipers (Cerastes). *Copeia*, *2003*(1), 131–137. https://doi.org/10.1643/0045-8511(2003)003[0131:VBITSS]2.0.CO;2

Young, B. A., & Morain, M. (2003). Vertical burrowing in the Saharan sand vipers (Cerastes). *Copeia*, *2003*(1), 131–137. https://doi.org/10.1643/0045-8511(2003)003[0131:VBITSS]2.0.CO;2

Zhang, T., & Goldman, D. I. (2014). The effectiveness of resistive force theory in granular locomotiona). *Physics of Fluids*, *26*(10), 101308. https://doi.org/10.1063/1.4898629